LISA capture sources: Approximate waveforms, signal-to-noise ratios, and parameter estimation accuracy

Leor Barack

Department of Physics and Astronomy and Center for Gravitational Wave Astronomy, University of Texas at Brownsville, Brownsville, Texas 78520, USA

Curt Cutler

Max-Planck-Institut fuer Gravitationsphysik, Albert-Einstein-Institut, Am Muehlenberg 1, D-14476 Golm bei Potsdam, Germany
(Received 29 October 2003; published 30 April 2004)

Captures of stellar-mass compact objects (COs) by massive ($\sim 10^6 M_\odot$) black holes (MBHs) are potentially an important source for LISA, the proposed space-based gravitational-wave (GW) detector. The orbits of the inspiraling COs are highly complicated; they can remain rather eccentric up until the final plunge, and display extreme versions of relativistic perihelion precession and Lense-Thirring precession of the orbital plane. The amplitudes of the strongest GW signals are expected to be roughly an order of magnitude smaller than LISA's instrumental noise, but in principle (i.e., with sufficient computing power) the GW signals can be disentangled from the noise by matched filtering. The associated template waveforms are not yet in hand, but theorists will very likely be able to provide them before LISA launches. Here we introduce a family of approximate (post-Newtonian) capture waveforms, given in (nearly) analytic form, for use in advancing LISA studies until more accurate versions are available. Our model waveforms include most of the key qualitative features of true waveforms, and cover the full space of capture-event parameters (including orbital eccentricity and the MBH's spin). Here we use our approximate waveforms to (i) estimate the relative contributions of different harmonics (of the orbital frequency) to the total signal-to-noise ratio, and (ii) estimate the accuracy with which LISA will be able to extract the physical parameters of the capture event from the measured waveform. For a typical source (a $10 M_\odot$ CO captured by a $10^6 M_\odot$ MBH at a signal-to-noise ratio of 30), we find that LISA can determine the MBH and CO masses to within a fractional error of $\sim 10^{-4}$, measure S/M^2 (where S and M are the MBH's mass and spin) to within $\sim 10^{-4}$, and determine the location to the source on the sky to within $\sim 10^{-3}$ stradians.

I. INTRODUCTION

Captures of stellar-mass compact objects (COs) by massive ($\sim 10^6 M_\odot$) black holes (MBHs) in galactic nuclei represent an important potential source for the Laser Interferometer Space Antenna (LISA), the proposed space-based gravitational-wave (GW) detector [1]. The capture orbits, which can remain rather eccentric right up to the final plunge, display extreme versions of relativistic perihelion precession and Lense-Thirring precession (i.e., precession of the orbital plane due to the spin of the MBH), as well as orbital decay. Ryan [2] has illustrated how the measured waveforms can effectively map out the spacetime geometry close to the MBH.

Rate estimates indicate that the strongest detectable sources will be $D \sim 1$ Gpc from us [3], implying the measured GW strain amplitude $h(t)$ will be roughly an order of magnitude smaller than the strain amplitude $n(t)$ due to detector noise. Nevertheless, because the capture waveform will be "visible" to LISA for $\sim 10^5$ cycles, in principle (i.e., with infinite computing power) it should be possible to dig these signals out of the noise using matched filtering. While until now, theorists have not been able to calculate capture waveforms with the accuracy required for matched filtering, great progress has been made on this problem in recent years (see the recent review by Poisson [4] and references therein),

and it seems very likely that sufficiently-accurate template waveforms *will* be available before LISA's planned launch in ~ 2011.

Nevertheless, there are many theoretical issues related to captures that must be addressed even *before* sufficiently accurate templates are in hand, as the final LISA mission specs are being driven substantially by the requirement that LISA be sensitive enough to see captures (see the LISA Science Requirements Document at the *LISA Sources and Data Analysis team* website [5]). Among the most pressing questions is how to efficiently search through the data for capture signals. Given the large dimensionality of the space of capture waveforms, and the length and complexity of the individual template signals, it is clear that straightforward matched filtering—using a huge set of templates that cover parameter space like a net—would require vastly more computational power than is practical. Instead, we need to develop suboptimal alternatives to coherent match filtering and to estimate the sensitivity of LISA *when using these methods*.

This is the first in a series of papers designed to address such data analysis problems, for LISA capture sources. Here we introduce a family of relatively simple inspiral waveforms, given in nearly analytic form [i.e., up to solutions of ordinary differential equations (ODEs)], that should roughly approximate the true waveforms and that include their key qualitative features. Because our approximate waveforms are

given in (nearly) analytic form, we can generate vast numbers of templates extremely fast—a feature that we expect to be crucial in performing Monte Carlo studies of search techniques.

Our capture waveforms are based on the lowest-order, quadrupolar waveforms for eccentric-orbit binaries derived by Peters and Matthews [6], but the orbits are corrected to include the effects of pericenter precession, Lense-Thirring precession, and inspiral from radiation reaction [all calculated using post-Newtonian (PN) formulas]. Our waveforms have the right dimensionality (except that in practice we will neglect the spin of the CO) and the same qualitative features as the true waveforms, except (i) they do not exhibit the extreme "zoom-whirl" behavior of true fully-relativistic waveforms just prior to plunge [7,8], and (ii) they approximate as constant the angle λ between the CO's orbital angular momentum and the MBH's spin, whereas the correct evolution would show a small secular change in λ. However, we do not expect these two (missing) effects to be very important for our purpose, since, again, the latter is small (at least for circular orbits [9]), while extreme zoom-whirl behavior occurs only for rather eccentric orbits extremely close to plunge. [The number of "whirls" per "zoom" grows only as $-\ln(p-p_s)$ as the orbit's semi-latus rectum p approaches the plunge value p_s [7,8], and so stretches of waveform exhibiting extreme zoom-whirl behavior will likely contribute only a very small fraction of the total signal-to-noise ratio (SNR).]

In this paper, we use our approximate waveforms to take a first cut at estimating the accuracy with which LISA should be able to extract the capture source's physical parameters, including its distance and location on the sky, the masses of both bodies, and the spin of the MBH. We also illustrate in detail the relative contributions of different harmonics (of the orbital frequency) to the total SNR of the waveform. For these calculations, besides using approximate waveforms, we also use a low-frequency approximation to the LISA response function and an approximate version of the Fisher-matrix inner product. Since our methods are so approximate, the results should be considered illustrative rather than definitive.

The plan of this paper is as follows. In Sec. II, to put the present work in context, we briefly summarize the previous literature on this topic and indicate the several areas of active theoretical research. In Sec. III we present our approximate, (nearly) analytic waveforms. Our scheme for incorporating the LISA response function and the noise closely follows Cutler [10], but we give enough detail that the reader could easily employ the response function detailed in Cornish and Rubbo [11] (which is more accurate at high frequencies). Section IV provides a brief review of signal analysis, partly to explain our conventions. In Sec. V we display plots showing the relative contributions of different harmonics to the total SNR. We show that, even for relatively modest final eccentricity, the higher harmonics contribute significantly. Finally, in Sec. VI, we present estimates of how accurately LISA can determine the physical parameters of capture systems. We emphasize that our treatment is highly modular, allowing for simple improvements of the various approximations.

A few details of our analysis are left to the Appendices. In Appendix A we derive a simple expression for the contribution to the pericenter precession from the spin of the MBH, and show its equivalence to the standard result. Appendix B compares the magnitudes of the various PN terms in our orbital evolution equations. Since the near-plunge capture orbits are highly relativistic, higher-order terms are comparable in magnitude to the lower-order ones, as one would expect. Estimates of the magnitudes of effects related to the CO's spin are given in Appendix C. The spin of the CO may have marginally important effects on the templates (for rapidly rotating COs), but for simplicity we leave these out of the rest of our analysis. (They could be put back in rather easily.)

In later papers will turn to the problem that is the main motivation for this work: designing a practical algorithm for digging capture waveforms out of the LISA noise. There we will use our approximate waveforms to estimate the scheme's sensitivity, compared to an optimal search with infinite computing power.

Our index notation is the following. Indices for vectors and tensors on parameter space are chosen from the beginning of the Latin alphabet $(a,b,c,\dots)$. Vectors and tensors on three-dimensional space have indices chosen from the middle of the Latin alphabet $(i,j,k,\dots)$, and run over 1,2,3; their indices are raised and lowered with the flat 3-metric, η_{ij}. We use Greek indices $(\alpha,\beta,\dots)$, running only over I,II, to label the two independent gravitational waveforms that LISA effectively generates. (No four-dimensional, spacetime indices occur in this paper.)

Throughout this paper we use units in which $G=c=1$.

II. SUMMARY OF PREVIOUS AND ONGOING THEORETICAL WORK

Most, if not all, nucleated galaxies harbor MBHs in their centers [12,13]. The MBH's gravity dominates the local stellar dynamics within a cusp radius $r_c=M/\sigma_c^2$, where M is the MBH mass and σ_c is the one-dimensional velocity dispersion of stars inside the cusp. A typical MBH with $M=10^6 M_\odot$ would have $r_c \sim 1$ pc. The total mass of stars inside the cusp is typically of order the MBH mass [3]. Captures occur when two stars in the cusp undergo a close encounter, sending one of them into the "loss cone." These are orbits that pass sufficiently close to the MBH that the timescale on which the CO tends to spiral into the MBH due to gravitational radiation reaction is shorter than the time scale on which the CO is scattered back out by other stars.

Because LISA's sensitivity band is centered at $f \sim 3 \times 10^{-3}$ Hz, the MBHs most "visible" to LISA are those with mass $M \sim 10^6 M_\odot$. To avoid tidal disruption, while being close enough to the MBH to emit GWs in the LISA frequency band, the captured star must be either a white dwarf (WD), neutron star (NS), black hole (BH), or a very low mass main-sequence star (LMMS) [3].

Early estimates of capture rates and LISA SNRs were made by Hils and Bender [14], who considered the capture of $1 M_\odot$ objects. More recent rate estimates [3] suggest that, while the total capture rate is dominated by LMMSs and

WDs, LISA's detection rate should be dominated by captures of $\sim 10 M_\odot$ BHs. This is partly because the BHs, being more massive, can be "seen" to greater distance, and partly because two-body relaxation enhances the density of BHs nearer the MBH [15]. (Two-body stellar collisions tend to equalize kinetic energies, causing heavier stars to sink to the center of the cusp.)

The first extended look at data analysis for capture sources was taken by Finn and Thorne [16]. They simplified the problem by restricting to the case of circular, equatorial orbits, but for this case they were able to calculate the correct relativistic orbits and waveforms, and they showed how the LISA SNR accumulates over the last year of inspiral—during which typically $\sim 10^5$ GW cycles are emitted—for a range of CO masses and MBH masses and spins. Their plots illustrate the salient fact that, typically, the entire last year of inspiral contributes significantly to the SNR. This is because, one year before plunge, the CO is already quite close to the MBH. Indeed, we shall see below that considerable signal-to-noise can accumulate even *before* the final year.

A more realistic treatment of the capture problem must incorporate the facts that (i) capture orbits will generally be nonequatorial (i.e., the CO's orbital angular momentum will not be aligned with the spin of the MBH), and (ii) a fair fraction of the inspiraling orbits will remain moderately eccentric right up until the final plunge. The latter fact may seem surprising, since it is well known that gravitational radiation reaction tends to circularize orbits rather efficiently.[1] The point, however, is that when the COs enter the loss cone, their orbits are initially *extremely* eccentric: $1 - e_{\text{init}} \sim 10^{-6} - 10^{-3}$, typically, while the initial pericenter distance is only $r_{p,\text{init}} \sim 8 - 100 M$ [18]. Given the CO's initial trajectory, just after scattering into the loss cone, we would like to calculate the eccentricity at the last stable orbit, e_{LSO}. For nonspinning MBHs, at least, this is straightforward. We find that $e_{LSO} > 0.1$ if $r_{p,\text{init}} \lesssim 20.0 M$, $e_{LSO} > 0.2$ for $r_{p,\text{init}} \lesssim 12.8 M$, and $e_{LSO} > 0.3$ for $r_{p,\text{init}} \lesssim 9.2 M$. [These estimates were obtained as follows. In the test particle limit, let r_1 and r_2 be the turning points (pericenter and apocenter) of the radial motion, where r is the standard radial coordinate in Schwarzschild. Define p and e by $r_1 (\equiv r_p) = p/(1+e)$ and $r_2 = p/(1-e)$. Plunge occurs at $p/M = 6 + 2e_{LSO}$ [7]. Then p_{init} is given by

$$p_{\text{init}}/M = 6 + 2e_{LSO} + \frac{1}{M} \int_{e_{LSO}}^{1} \frac{dp}{de} de. \tag{1}$$

(Of course, the upper limit in the integral should actually be slightly less than 1.0—say, $e = 0.99995$—but since the integrand is smooth as $e \to 1.0$, it makes no practical difference if we simply approximate the upper limit as 1.0.) The derivative $dp/de = \dot{p}/\dot{e}$ due to radiation reaction was calculated numerically by Cutler, Kennefick, and Poisson [7] for orbits near the horizon. We used the results from Fig. 1 of [7] to integrate (roughly, using a pencil and ruler) dp/de backwards (in time) from plunge to $p/M = 12$. We then used the lowest-order post-Newtonian result [6] $dp/de = (12/19)(p/e)(1 + \frac{7}{8}e^2)/(1 + \frac{121}{304}e^2)$ to continue the integration backwards to $e = 1.0$.]

Based on Freitag's Monte Carlo simulation of capture events in our Galaxy (Fig. 1 of [18]), we then estimate that roughly half the captures of $\sim 10 M_\odot$ BHs (which, again, should dominate LISA's detection rate) should have $e_{LSO} \gtrsim 0.2$. Note that a year or two before the final plunge the eccentricity of such captures will, in fact, be significantly larger than e_{LSO} (as illustrated in Figs. 7, 8).

Capture sources are unlike some other LISA sources (e.g., galactic WD-WD binaries or MBH-MBH binaries at high redshift), in that they may lie quite near the margin of detectability, given LISA's current design specifications. (Put another way, a modest change in the height or location of the noise floor may determine whether or not these sources are detected.) Since detecting capture sources is very high priority for LISA, it has been a high priority for LISA's Sources and Data Analysis team ["Working Group 1" (WG1)] to make as much progress as possible studying capture sources before finalizing the LISA design [19]. This motivates current research on several fronts, including work to (i) improve estimates for event rates and for the distribution of source parameters (especially masses and initial pericenter distances); (ii) solve the radiation reaction problem to determine the true orbit, and construct the corresponding waveforms; (iii) investigate what science can be done with these sources (both astrophysics and tests of fundamental physics); (iv) understand the limits on capture detection due to "source confusion," i.e., the background "noise" caused by *other*, unresolved capture sources; and (v) construct strategies to dig the capture waveforms out of the instrumental and confusion noise. The present work addresses issues (iii) and (iv) above, while later papers will address problem (v).

Parameter estimation with LISA [clearly bearing on above issue (iii)] has been looked at systematically for WD-WD binaries by Peterseim *et al.* [20] and Cutler [10], and for mergers of MBH pairs by Cutler [10] and Vecchio [21]. No comparable analysis has yet been done for capture sources. For captures, some initial estimates of parameter estimation accuracy were made by Poisson [22] and Ryan [2] (the latter's main interest being to test alternative gravitation theories). However, both Poisson and Ryan used extremely simplifying approximations: they both took the inspiral orbits to be circular and equatorial *a priori* (effectively reducing the number of unknown system parameters, while leaving uninvestigated the significance of perihelion precession and Lense-Thirring precession for parameter extraction), and they did not incorporate in their signal models the amplitude and phase modulations that arise from LISA's orbital motion (which LISA will use to determine the source position). By comparison, our treatment is far more realistic. While our results are also approximate, we believe they should at least give correct order-of-magnitude estimates of LISA's parameter estimation accuracy (while it seems doubtful that the earlier estimates can be trusted even at that level).

---

[1] Except very close to plunge, where the very strong-field potential tends to decrease the rate of circularization, and may even reverse the sign of de/dt—cf. [7,17].

III. OUR MODEL INSPIRAL WAVEFORM

We approximate the CO-MBH system as being, at any instant, a Newtonian-orbit binary emitting a Peters-Matthews (i.e., lowest order, quadrupolar) waveform. We then use post-Newtonian (PN) equations to secularly evolve the parameters of the orbit. In particular, we include orbital decay from radiation reaction, pericenter precession, and Lense-Thirring precession of the orbital plane. The modulation of the waveform's amplitude and phase due to Lense-Thirring precession has been described (in the context of circular-orbit binaries) by Apostolatos *et al.* [23]. The motion of the LISA detector introduces additional modulations; our handling of these closely follows that of Cutler [10]. Cutler's treatment does not account for the decrease in LISA's sensitivity at frequencies $f \gtrsim 10$ mHz (where the GW wavelength is smaller than the detector's armlength)—an effect recently accounted for by Cornish and Rubbo [11]. It would be straightforward to repeat our analysis using the Cornish and Rubbo formalism. However, since most of the SNR for astophysically-relevant capture sources will accumulate at frequencies below ~ 10 mHz, we expect our high-frequency approximation will have only a modest impact on the results.

We emphasize that our treatment is highly modular. E.g., while our choice of physical variables is a slight generalization of the variables used in [23] and [10], it would be straightforward to re-write our waveforms using a parametrization along the lines of Buonanno, Chen, and Vallisneri [24] (hereafter, BCV), who found a particularly convenient way of parametrizing circular-orbit binaries with spin. (It seems the BCV parametrization should be readily extendible to eccentric orbits.) Similarly, it would be straightforward for us to treat the LISA noise and response function along the lines of Cornish and Rubbo [11]. We do not implement either of these treatments here because they did not seem of critical importance, and because our work was already well underway when they became available.

A. Principal axes

In this paper, we adopt a mixed notation for spatial vectors, sometimes labelling them with spatial indices $(i, j, k, \dots)$, but sometimes suppressing the indices and instead using the standard $3-d$ vector notation: an over-arrow (as in $\vec{A}$) to represent a vector, $\vec{A} \cdot \vec{B}$ to represent a scalar ("dot") product, and $\vec{A} \times \vec{B}$ to represent the vector ("cross") product. An overhat (as in $\hat{n}$) will indicate that a vector is normalized, i.e., has unit length. We trust our meaning will always be clear, despite this mixed notation.

Let $\hat{n}$ be the unit vector pointing from the detector to the source, and let $\hat{L}(t)$ be the unit vector along the CO's orbital angular momentum. We find it convenient to work in a (time-varying) wave frame defined with respect to $\hat{n}$ and $\hat{L}(t)$. We define unit vectors $\hat{p}$ and $\hat{q}$ by

$$\hat{p} \equiv (\hat{n} \times \hat{L})/|\hat{n} \times \hat{L}|,$$

$$\hat{q} \equiv \hat{p} \times \hat{n}, \tag{2}$$

based on which we then define the two polarization basis tensors

$$H_{ij}^{+}(t) \equiv \hat{p}_i \hat{p}_j - \hat{q}_i \hat{q}_j,$$

$$H_{ij}^{\times}(t) \equiv \hat{p}_i \hat{q}_j + \hat{q}_i \hat{p}_j. \tag{3}$$

The general GW strain field at the detector can then be written as

$$h_{ij}(t) = A^{+}(t) H_{ij}^{+}(t) + A^{\times}(t) H_{ij}^{\times}(t), \tag{4}$$

where $A^{+}(t)$ and $A^{\times}(t)$ are the amplitudes of the two polarizations.

B. Peters-Mathews waveforms

In the quadrupole approximation, the metric perturbation far from the source is given (in the "transverse-traceless" gauge) by [25]

$$h_{ij} = (2/D)\left(P_{ik}P_{jl} - \frac{1}{2}P_{ij}P_{kl}\right)\ddot{I}^{kl} \tag{5}$$

where D is the distance to the source, the projection operator P_{ij} is given by $P_{ij} \equiv \eta_{ij} - \hat{n}_i \hat{n}_j$, and $\ddot{I}^{ij}$ is the second time derivative of the inertia tensor. In this paper we work in the limit of small mass ratio, $\mu/M \ll 1$, where μ and M are the masses of the CO and MBH, respectively. In this limit, the inertia tensor is just $I^{ij}(t) = \mu r^i(t) r^j(t)$, where $\vec{r}$ is the position vector of the CO with respect to the MBH.

Consider now a CO-MBH system described as a Newtonian binary, with semi-major axis a, eccentricity e, and orbital frequency $\nu = (2\pi M)^{-1}(M/a)^{3/2}$. Let $\hat{e}_1$ and $\hat{e}_2$ be orthonormal vectors pointing along the major and minor axes of the orbital ellipse, respectively. Since the orbit is planar, I^{ij} has only 3 independent components: I^{11}, I^{21}, and I^{22}, and as the motion is periodic, we can express I^{ij} as a sum of harmonics of the orbital frequency ν: $I^{ij} = \Sigma_n I_n^{ij}$.

We next denote

$$a_n \equiv \frac{1}{2}(\ddot{I}_n^{11} - \ddot{I}_n^{22}),$$

$$b_n \equiv \ddot{I}_n^{12},$$

$$c_n \equiv \frac{1}{2}(\ddot{I}_n^{11} + \ddot{I}_n^{22}). \tag{6}$$

Peters and Matthews showed [6] that

$$a_n = -n\mathcal{A}[J_{n-2}(ne) - 2eJ_{n-1}(ne) + (2/n)J_n(ne)$$
$$+ 2eJ_{n+1}(ne) - J_{n+2}(ne)]\cos[n\Phi(t)],$$

$$b_n = -n\mathcal{A}(1-e^2)^{1/2}[J_{n-2}(ne) - 2J_n(ne)$$
$$+ J_{n+2}(ne)]\sin[n\Phi(t)],$$

$$c_n = 2\mathcal{A}J_n(ne)\cos[n\Phi(t)], \tag{7}$$

where

$$\mathcal{A} \equiv (2\pi\nu M)^{2/3}\mu, \tag{8}$$

J_n are Bessel functions of the first kind, and $\Phi(t)$ is the mean anomaly (measured from pericenter). For a strictly Newtonian binary we have

$$\Phi(t) = 2\pi\nu(t - t_0) + \Phi_0, \tag{9}$$

where Φ_0 is the mean anomaly at t_0. Decomposing Eq. (4) into n-harmonic contributions and using Eq. (5), one then easily obtains explicit expressions for the n-harmonic components of the two polarization coefficients, $A^+ \equiv \Sigma_n A_n^+$ and $A^- \equiv \Sigma_n A_n^-$. They are

$$A_n^+ = -[1 + (\hat{L} \cdot \hat{n})^2][a_n\cos(2\gamma) - b_n\sin(2\gamma)]$$
$$+ [1 - (\hat{L} \cdot \hat{n})^2]c_n,$$

$$A_n^\times = 2(\hat{L} \cdot \hat{n})[b_n\cos(2\gamma) + a_n\sin(2\gamma)], \tag{10}$$

where γ is an azimuthal angle measuring the direction of pericenter with respect to $\hat{x} \equiv [-\hat{n} + \hat{L}(\hat{L} \cdot \hat{n})]/[1 - (\hat{L} \cdot \hat{n})^2]^{1/2}$.

C. LISA's response function

With its three arms, LISA functions as a pair of two-arm detectors, outputting two orthogonal signals. Let l_1^i, l_2^i, l_3^i be unit vectors, each along one of LISA's three arms, and let L be LISA's average arm length. Let also $L_i(t)$ be the length of the i'th arm when LISA measures an incident GW, and denote $\delta L_1(t) \equiv L_i(t) - L$. We refer to the two-arm detector formed by arms 1 and 2 as "detector I." The strain amplitude in this detector is given by

$$h_I(t) \equiv [\delta L_1(t) - \delta L_2(t)]/L = \frac{1}{2}h_{ij}(t)(l_1^i l_1^j - l_2^i l_2^j). \tag{11}$$

The second, orthogonal signal is then given by [10]

$$h_{II}(t) = 3^{-1/2}[\delta L_1(t) + \delta L_2(t) - 2\delta L_3(t)]/L$$
$$= \frac{1}{2\sqrt{3}}h_{ij}(t)(l_1^i l_1^j + l_2^i l_2^j - 2l_3^i l_3^j). \tag{12}$$

For GW wavelengths much larger than the LISA arm length, $h_I(t)$ and $h_{II}(t)$ coincide with the two "Michelson variables" [26], describing the responses of a pair of two-arm/90° detectors. We can then write $h_I(t)$ and $h_{II}(t)$ as a sum over n-harmonic contributions,

$$h_\alpha(t) = \sum_n h_{\alpha,n}(t) \quad (\alpha = I, II), \tag{13}$$

where

$$h_{\alpha,n}(t) = \frac{1}{D}\frac{\sqrt{3}}{2}[F_\alpha^+(t)A_n^+(t) + F_\alpha^\times(t)A_n^\times(t)]. \tag{14}$$

Here $A_n^{+,\times}(t)$ are the two polarization coefficients [given, in our model, by Eq. (10) above], the factor $\sqrt{3}/2$ accounts for the fact that the actual angle between LISA arms is 60° rather than 90°, and $F_\alpha^{+,\times}$ are the "antenna pattern" functions, reading [23,27]

$$F_I^+ = \frac{1}{2}(1 + \cos^2\theta)\cos(2\phi)\cos(2\psi)$$
$$- \cos\theta\sin(2\phi)\sin(2\psi),$$

$$F_I^\times = \frac{1}{2}(1 + \cos^2\theta)\cos(2\phi)\sin(2\psi)$$
$$+ \cos\theta\sin(2\phi)\cos(2\psi), \tag{15a}$$

$$F_{II}^+ = \frac{1}{2}(1 + \cos^2\theta)\sin(2\phi)\cos(2\psi)$$
$$+ \cos\theta\cos(2\phi)\sin(2\psi),$$

$$F_{II}^\times = \frac{1}{2}(1 + \cos^2\theta)\sin(2\phi)\sin(2\psi)$$
$$- \cos\theta\cos(2\phi)\cos(2\psi). \tag{15b}$$

In these expressions, (θ, ϕ) is the source's sky location in a detector-based coordinate system and ψ is the "polarization angle" describing the orientation of the "apparent ellipse" drawn by the projection of the orbit on the sky—see Fig. 1 in Ref. [23] and the explicit relation (17) given below.

It is more convenient to express the above response function in terms of angles defined not in the rotating, detector-based system, but rather in a fixed, ecliptic-based coordinate system. The angles θ, ϕ are related to θ_S, ϕ_S—the source location in an ecliptic-based system—through

$$\cos\theta(t) = \frac{1}{2}\cos\theta_S - \frac{\sqrt{3}}{2}\sin\theta_S\cos[\bar{\phi}_0 + 2\pi(t/T) - \phi_S],$$

$$\phi(t) = \bar{\alpha}_0 + 2\pi(t/T)$$
$$+ \tan^{-1}\left[\frac{\sqrt{3}\cos\theta_S + \sin\theta_S\cos[\bar{\phi}_0 + 2\pi(t/T) - \phi_S]}{2\sin\theta_S\sin[\bar{\phi}_0 + 2\pi(t/T) - \phi_S]}\right], \tag{16}$$

where $T = 1$ year and $\bar{\phi}_0, \bar{\alpha}_0$ are constant angles specifying, respectively, the orbital and rotational phase of the detector at $t = 0$. (See Cutler [10] for a complete definition of these angles; note, though, that the angle $\bar{\alpha}_0 = 0$ in this paper is referred to as $\alpha_0 = 0$ in Cutler [10].)

Next, we express the polarization angle ψ in terms of θ_S, ϕ_S and θ_L, ϕ_L—the direction of the CO's orbital angular momentum, $\hat{L}(t)$, in the ecliptic-based system. We have

$$\tan \psi = \left\{ \frac{1}{2}\cos\theta_L - \frac{\sqrt{3}}{2}\sin\theta_L\cos[\bar{\phi}_0 + 2\pi(t/T) - \phi_L] - \cos\theta(t)[\cos\theta_L\cos\theta_S + \sin\theta_L\sin\theta_S\cos(\phi_L - \phi_S)] \right\} \Big/$$

$$\left[\frac{1}{2}\sin\theta_L\sin\theta_S\sin(\phi_L - \phi_S) - \frac{\sqrt{3}}{2}\cos(\bar{\phi}_0 + 2\pi t/T)(\cos\theta_L\sin\theta_S\sin\phi_S - \cos\theta_S\sin\theta_L\sin\phi_L) \right.$$

$$\left. - \frac{\sqrt{3}}{2}\sin(\bar{\phi}_0 + 2\pi t/T)(\cos\theta_S\sin\theta_L\cos\phi_L - \cos\theta_L\sin\theta_S\cos\phi_S) \right]. \tag{17}$$

For concreteness we shall hereafter take $\bar{\phi}_0 = \bar{\alpha}_0 = 0$, but one could specify any other value as appropriate.

Note that the angles θ_L, ϕ_L are not constant, since $\hat{L}$ precesses about the MBH's spin direction $\hat{S}$. Let θ_K, ϕ_K be the direction of $\vec{S}$ in the ecliptic-based system ("K" standing for "Kerr"); let also λ be the angle *between* $\hat{L}$ and $\hat{S}$, and $\alpha(t)$ be an azimuthal angle (in the orbital plane) that measures the precession of $\hat{L}$ around $\hat{S}$: Specifically, let

$$\hat{L} = \hat{S}\cos\lambda + \frac{\hat{z} - \hat{S}\cos\theta_K}{\sin\theta_K}\sin\lambda\cos\alpha + \frac{\hat{S}\times\hat{z}}{\sin\theta_K}\sin\lambda\sin\alpha, \tag{18}$$

where $\hat{z}$ is a unit vector normal to the ecliptic. Then the angles $\theta_L(t), \phi_L(t)$ are given in terms of $\theta_K, \phi_K, \lambda, \alpha(t)$ as

$$\cos\theta_L(t) = \cos\theta_K\cos\lambda + \sin\theta_K\sin\lambda\cos\alpha(t),$$

$$\sin\theta_L(t)\cos\phi_L(t) = \sin\theta_K\cos\phi_K\cos\lambda$$
$$- \cos\phi_K\cos\theta_K\sin\lambda\cos\alpha(t)$$
$$+ \sin\phi_K\sin\lambda\sin\alpha(t),$$

$$\sin\theta_L(t)\sin\phi_L(t) = \sin\theta_K\sin\phi_K\cos\lambda$$
$$- \sin\phi_K\cos\theta_K\sin\lambda\cos\alpha(t)$$
$$- \cos\phi_K\sin\lambda\sin\alpha(t). \tag{19}$$

D. The pericenter angle $\tilde{\gamma}$

As mentioned above, the angle γ that appears in Eqs. (10) measures the direction of pericenter with respect to $\hat{x} \equiv [-\hat{n} + \hat{L}(\hat{L}\cdot\hat{n})]/[1 - (\hat{L}\cdot\hat{n})^2]^{1/2}$. With this definition, γ is neither purely extrinsic nor purely intrinsic. (In the terminology of BCV, "intrinsic" parameters describe the system without reference to the location or orientation of the observer.) We will find it convenient to introduce a somewhat

TABLE I. Summary of physical parameters and their meaning. The angles (θ_S, ϕ_S) and (θ_K, ϕ_K) are associated with a spherical coordinate system attached to the ecliptic. $\hat{L}$ and $\hat{S}$ are unit vectors in the directions of the orbital angular momentum and the MBH's spin, respectively. For further details see Fig. 1 and the description in the text.

|		
λ^0	t_0	t_0 is time where orbital frequency sweeps through fiducial value (e.g., 1 mHz)
λ^1	$\ln\mu$	(ln of) CO's mass
λ^2	$\ln M$	(ln of) MBH's mass
λ^3	S/M^2	magnitude of (specific) spin angular momentum of MBH
λ^4	e_0	$e(t_0)$, where $e(t)$ is the orbital eccentricity
λ^5	$\tilde{\gamma}_0$	$\tilde{\gamma}(t_0)$, where $\tilde{\gamma}(t)$ is the angle (in orbital plane) between $\hat{L}\times\hat{S}$ and pericenter
λ^6	Φ_0	$\Phi(t_0)$, where $\Phi(t)$ is the mean anomaly
λ^7	$\mu_S \equiv \cos\theta_S$	(cosine of) the source direction's polar angle
λ^8	ϕ_S	azimuthal direction to source
λ^9	$\cos\lambda$	$\hat{L}\cdot\hat{S}(=\text{const})$
λ^{10}	α_0	$\alpha(t_0)$, where $\alpha(t)$ is the azimuthal direction of $\hat{L}$ (in the orbital plane)
λ^{11}	$\mu_K \equiv \cos\theta_K$	(cosine of) the polar angle of MBH's spin
λ^{12}	ϕ_K	azimuthal direction of MBH's spin
λ^{13}	$\ln(\mu/D)$	(ln of) CO's mass divided by distance to source
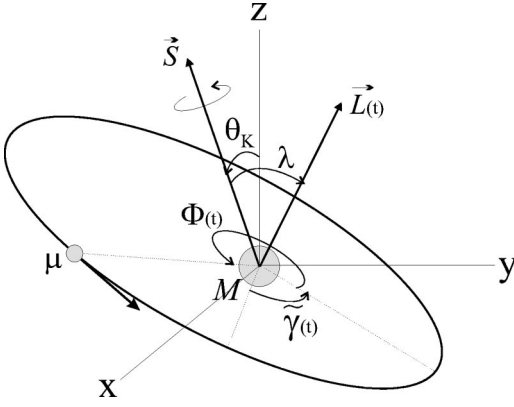
FIG. 1. The MBH-CO system: setup and notation. M and μ are the masses of the MBH and the CO, respectively. The axes labeled x-y-z represent a Cartesian system *based on ecliptic coordinates* (the Earth's motion around the Sun is in the x-y plane). The spin $\vec{S}$ of the MBH is parametrized by its magnitude S and the two angular coordinates θ_K, ϕ_K, defined (in the standard manner) based on the system x-y-z. $\vec{L}(t)$ represents the (time-varying) orbital angular momentum; its direction is parametrized by the (constant) angle λ between $\vec{L}$ and $\vec{S}$, and by an azimuthal angle $\alpha(t)$ (not shown in the figure). The angle $\tilde{\gamma}(t)$ is the (intrinsic) direction of pericenter, as measured with respect to $\hat{L} \times \hat{S}$. Finally, $\Phi(t)$ denotes the mean anomaly of the orbit, i.e., the average orbital phase with respect to the direction of pericenter.

different convention for the zero point of this angle: We shall define $\tilde{\gamma}$ to be the direction of pericenter with respect to $\hat{L} \times \hat{S}$. Then $\tilde{\gamma}$ is a purely intrinsic quantity.

Clearly, γ and $\tilde{\gamma}$ are related by

$$\gamma = \tilde{\gamma} + \beta, \tag{20}$$

where β is the angle from $\hat{x} \propto [\hat{L}(\hat{L} \cdot \hat{n}) - \hat{n}]$ to $(\hat{L} \times \hat{S})$. It is straightforward to show that β is given by

$$\sin \beta = \frac{\cos \lambda \hat{L} \cdot \hat{n} - \hat{S} \cdot \hat{n}}{\sin \lambda [1 - (\hat{L} \cdot \hat{n})^2]^{1/2}},$$

$$\cos \beta = \frac{\hat{n} \cdot (\hat{S} \times \hat{L})}{\sin \lambda [1 - (\hat{L} \cdot \hat{n})^2]^{1/2}}. \tag{21}$$

To evaluate $\beta(t)$ in practice, we shall need the following relations:

$$\hat{S} \cdot \hat{n} = \cos \theta_S \cos \theta_K + \sin \theta_S \sin \theta_K \cos(\phi_S - \phi_K), \tag{22}$$

$$\hat{n} \cdot (\hat{S} \times \hat{L}) = \sin \theta_S \sin(\phi_K - \phi_S) \sin \lambda \cos \alpha$$

$$+ \frac{\hat{S} \cdot \hat{n} \cos \theta_K - \cos \theta_S}{\sin \theta_K} \sin \lambda \sin \alpha, \tag{23}$$

and

$$\hat{L} \cdot \hat{n} = \hat{S} \cdot \hat{n} \cos \lambda + \frac{\cos \theta_S - \hat{S} \cdot \hat{n} \cos \theta_K}{\sin \theta_K} \sin \lambda \cos \alpha$$

$$+ \frac{(\hat{S} \times \bar{z}) \cdot \hat{n}}{\sin \theta_K} \sin \lambda \sin \alpha, \tag{24}$$

or, equivalently,

$$\hat{L} \cdot \hat{n} = \cos \theta_S \cos \theta_L + \sin \theta_S \sin \theta_L \cos(\phi_S - \phi_L). \tag{25}$$

Note that the time variation of $\hat{S} \cdot \hat{n}$ is very small in the extreme mass-ratio case considered here: this quantity is constant to better than $\sim (\mu/M)(S/M^2)$ (see Appendix C). In our model we shall approximate $\hat{S}$—and hence $\hat{S} \cdot \hat{n}$—as strictly constant.

E. Parameter space

The two-body system is described by 17 parameters. The spin of the CO can be marginally relevant (see Appendix C), but in this paper we shall ignore it, leaving us with 14 parameters. We shall denote a vector in the 14D parameter space by λ^a ($a = 0, \ldots, 13$). We choose our parameters as follows:

$$\lambda^a \equiv (\lambda^0, \ldots, \lambda^{13}) = [t_0 \ln \mu, \ln M, S/M^2, e_0, \tilde{\gamma}_0, \Phi_0, \mu_S$$

$$\equiv \cos \theta_S, \phi_S, \cos \lambda, \alpha_0, \mu_K \equiv \cos \theta_K, \phi_K, \ln(\mu/D)]. \tag{26}$$

Here t_0 is a time parameter that allows us to specify "when" the inspiral occurs—we shall generally choose t_0 to be the instant of time when the (radial) orbital frequency sweeps through some fiducial value ν_0 (typically, we shall choose ν_0 of order 1 mHz), μ and M are the masses of the CO and MBH, respectively, and S is the magnitude of the MBH's spin angular momentum (so $0 \leq S/M^2 \leq 1$). The parameters e_0, $\tilde{\gamma}_0$, and Φ_0 describe, respectively, the eccentricity, the direction of the pericenter within the orbital plane, and the mean anomaly—all at time t_0. More specifically, we take $\tilde{\gamma}_0$ to be the angle (in the plane of the orbit) from $\hat{L} \times \hat{S}$ to pericenter, and, as usual, Φ_0 to be the mean anomaly with respect to pericenter passage. The parameter $\alpha_0 \equiv \alpha(t = t_0)$ [where $\alpha(t)$ is defined in Eq. (18)] describes the direction of $\hat{L}$ around $\hat{S}$ at t_0. The angles (θ_S, ϕ_S) are the direction to the source, in ecliptic-based coordinates; (θ_K, ϕ_K) represent the direction $\hat{S}$ of the MBH's spin (approximated as constant) in ecliptic-based coordinates; and λ is the angle between $\hat{L}$ and $\hat{S}$ (also approximated as constant[2]). Finally, D is the distance to the source.

---

[2] In reality, radiation reaction will impose a small time variation in λ; however, this variation is known to be very small (see Ref. [9]) and we shall ignore it here. When a model of the time-variation of λ is eventually at hand, it would be trivial to generalize our treatment to incorporate it: one would just need an equation for $d\lambda/dt$, and in the parameter list λ would be replaced by λ_0—the value of λ at time t_0.

The various parameters and their meaning are summarized in Table I. Figure 1 illustrates the various angles involved in our parametrization.

Note for simplicity we are treating the background spacetime as Minkowski space, not Robertson-Walker. To correct this, for a source at redshift z, requires only the simple translation: $M \to M(1+z)$, $\mu \to \mu(1+z)$, $S \to S(1+z)^2$, $D \to D_L$, where D_L is the "luminosity distance" [28].

The parameters can be divided into "intrinsic" and "extrinsic" parameters, following BCV. Extrinsic parameters refer to the observer's position or orientation, or to the zero-of-time on the observer's watch. There are seven extrinsic parameters: the four parameters t_0, μ_S, ϕ_S, and D corre-spond to the freedom to translate the same binary in space and time, and the three parameters μ_K, ϕ_K, and α_0 are basically Euler angles that specify the orientation of the orbit with respect to the observer (at t_0). The intrinsic parameters are the ones that control the detailed dynamical evolution of the system, without reference to the observer's location or orientation. In our parametrization, the seven intrinsic parameters are $\ln \mu$, $\ln M$, S/M^2, $\cos \lambda$, e_0, $\tilde{\gamma}_0$, and Φ_0. BCV observed (in the context of circular-orbit binaries with spin) that extrinsic parameters are generally much "cheaper" to search over than intrinsic parameters. We shall make good use of this important observation in further papers.

F. Orbital evolution equations

We evolve $\Phi(t)$, $\nu(t)$, $\tilde{\gamma}(t)$, $e(t)$, and $\alpha(t)$ using the following PN formulas:

$$\frac{d\Phi}{dt} = 2\pi\nu, \tag{27}$$

$$\frac{d\nu}{dt} = \frac{96}{10\pi}(\mu/M^3)(2\pi M\nu)^{11/3}(1-e^2)^{-9/2}\{[1+(73/24)e^2+(37/96)e^4](1-e^2)$$
$$+ (2\pi M\nu)^{2/3}[(1273/336)-(2561/224)e^2-(3885/128)e^4-(13147/5376)e^6]$$
$$- (2\pi M\nu)(S/M^2)\cos\lambda(1-e^2)^{-1/2}[(73/12)+(1211/24)e^2+(3143/96)e^4+(65/64)e^6]\}, \tag{28}$$

$$\frac{d\tilde{\gamma}}{dt} = 6\pi\nu(2\pi\nu M)^{2/3}(1-e^2)^{-1}\left[1+\frac{1}{4}(2\pi\nu M)^{2/3}(1-e^2)^{-1}(26-15e^2)\right]$$
$$- 12\pi\nu\cos\lambda(S/M^2)(2\pi M\nu)(1-e^2)^{-3/2}, \tag{29}$$

$$\frac{de}{dt} = -\frac{e}{15}(\mu/M^2)(1-e^2)^{-7/2}(2\pi M\nu)^{8/3}$$
$$\times \left[(304+121e^2)(1-e^2)(1+12(2\pi M\nu)^{2/3})-\frac{1}{56}(2\pi M\nu)^{2/3}((8)(16705)+(12)(9082)e^2-25211e^4)\right]$$
$$+ e(\mu/M^2)(S/M^2)\cos\lambda(2\pi M\nu)^{11/3}(1-e^2)^{-4}[(1364/5)+(5032/15)e^2+(263/10)e^4], \tag{30}$$

$$\frac{d\alpha}{dt} = 4\pi\nu(S/M^2)(2\pi M\nu)(1-e^2)^{-3/2}. \tag{31}$$

Equations (28), (29), and (30) are from Junker and Schäfer [29], except (i) the second line of Eq. (29) is from Brumberg [30] (cf. our Appendix A), and the last term in Eq. (28)—the term $\propto S/M^2$—is from Ryan [31]. Equation (31) is from Barker and O'Connell [32]. The dissipative terms $d\nu/dt$ and de/dt are given accurately through 3.5PN order (i.e., one order higher than 2.5PN order, where radiation reaction first becomes manifest).[3] The nondissipative equations, for $d\tilde{\gamma}/dt$ and $d\alpha/dt$, are accurate through 2PN order.[4]

---

[3]The currently undetermined term in the 3.5PN expressions [see [33], in particular Eqs. (12)–(14) therein] does not show up in our calculation, since here we are ignoring terms that are higher-order in the mass ratio μ/M.

[4]In fact, the equations for $d\tilde{\gamma}/dt$ and $d\alpha/dt$ are missing terms proportional to $(S/M^2)^2$, which, according to usual "order counting" are classified as 2PN. However, this usual counting is misleading when the central object is a spinning BH: Because BHs are ultracompact, their spins are smaller than suggested by the usual counting, and the missing terms $\propto(S/M^2)^2$ have, in fact, the same magnitude as 3PN terms. Similarly, the terms $\propto(S/M^2)$ in Eqs. (29) and (31) can be viewed as effectively 1.5PN terms.
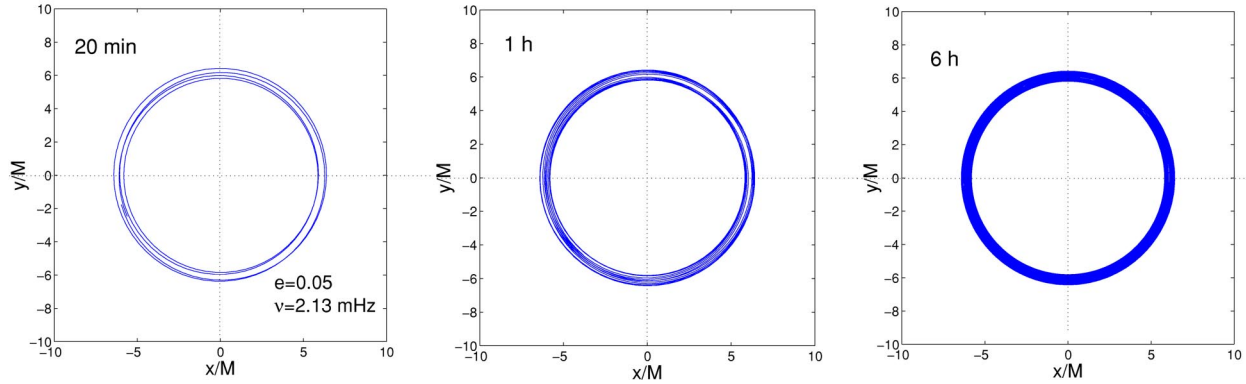
FIG. 2. Sample equatorial orbits: Shown (left to right, respectively) are 20 minutes, 1 hour, and 6 hours-long samples of the CO's trajectory just before approaching the LSO. (x, y) is a Cartesian coordinate system in the orbital (equatorial) plane, centered at the MBH. The axes give the distance in units of the MBH's mass M. This sequence of plots shows a case with a very small LSO eccentricity, $e = 0.05$. The other physical parameters are set as follows: CO's mass: $\mu = 10 M_\odot$; MBH's mass: $M = 10^6 M_\odot$; MBH's spin magnitude: $S = M^2$.

In solving the above time-evolution equations, the initial values (at time t_0) of Φ, ν, $\tilde{\gamma}$, e, and α are just the parameters Φ_0, ν_0, $\tilde{\gamma}_0$, e_0, and α_0.

We emphasize again that our treatment is highly modular: The PN expressions in Eqs. (28)–(31) could be replaced with improved ones as soon as higher-order PN expressions are available. Also, one might wish to improve these evolution equations using values from look-up tables, or results from numerical studies of the orbital evolution in Kerr (such as in [9]).

G. Doppler phase modulation

Doppler phase modulation due to LISA's orbital motion becomes important for integration times longer than a few weeks. We incorporate this effect by shifting the phase $\Phi(t)$, according to

$$\Phi(t) \to \Phi(t) + \Phi^D(t), \tag{32}$$

where

$$\Phi^D(t) = 2\pi\nu(t)R\sin\theta_S\cos[2\pi(t/T) - \phi_S]. \tag{33}$$

Here $R \equiv 1$ AU $= 499.00478$ sec.

H. Putting the pieces together

The algorithm for constructing our approximate waveform is then: Fix some fiducial frequency ν_0 and choose waveform parameters $(t_0, \ln\mu, \ln M, S/M^2, e_0, \tilde{\gamma}_0, \Phi_0, \cos\theta_S, \phi_S, \cos\lambda, \alpha_0, \cos\theta_K, \phi_K, D)$. Solve the ODEs (27)–(31) for $\Phi(t)$, $\nu(t)$, $\tilde{\gamma}(t)$, $e(t)$, $\alpha(t)$. Calculate $\theta_L(t), \phi_L(t)$ using Eqs. (19) and then obtain $\psi(t)$ from Eq. (17). Calculate $\gamma(t)$ from $\tilde{\gamma}(t)$ using Eqs. (20) and (21). Use $e(t)$ and $\nu(t)$ to calculate $a_n(t), b_n(t), c_n(t)$ in Eqs. (7), remembering to include the Doppler modulation via $n\Phi(t) \to n[\Phi(t) + \Phi^D(t)]$, in the manner of Eqs. (32) and (33). Calculate the amplitude coefficients $A_n^{+,\times}$ and the antenna pattern functions $F_\alpha^{+,\times}$ using Eqs. (10) and (15), respectively. Then finally calculate $h_\alpha(t)$ (for $\alpha = I, II$) using Eqs. (14) and (13).

Note that, in our treatment, pericenter precession and Lense-Thirring precession have no effect on the intrinsic signal (the signal in a frame that rotates with the system), since we always use the Peters-Matthews ''lowest-order'' waveforms. The effect of these motions is simply to rotate the binary system with respect to the detector. This relative rotation modulates the polarization angle ψ [which appears in the response functions $F_\alpha^{+,\times}(t)$] since ψ depends on $\hat{L}$, and it affects the amplitudes $A^{+,\times}$ since the latter depend on $\hat{L} \cdot \hat{n}$ and γ.

Figures 2–6 show some sample orbits and waveforms, obtained from employing the above algorithm. Figures 7 and 8 demonstrate the evolution of orbits in the eccentricity-frequency plane.

IV. FORMALISM OF SIGNAL ANALYSIS

This section briefly reviews the basic formulas of signal analysis, with application to LISA. We follow closely the treatment of Cutler [10]. In particular, our analysis is strictly valid only in the low-frequency regime, where the light-travel-time up and down one arm is much less than the gravitational wave period. (However, we expect it to be a reasonable approximation at higher frequencies as well.)

As discussed above, LISA functions as a pair of two-arm, Michelson detectors, which we label I and II. The output from these two detectors can be represented by the vector $s_\alpha(t)$ (with $\alpha = I, II$). In what follows it will be convenient to work with the Fourier transform of the signal; the convention we use is

$$\tilde{s}_\alpha(f) \equiv \int_{-\infty}^{\infty} e^{2\pi i f t} s_\alpha(t) dt. \tag{34}$$

Now, the output $s_\alpha(t)$ is the sum of incident gravitational waves $h_\alpha(t)$ and instrumental noise $n_\alpha(t)$. For simplicity we assume that (i) the noise is stationary and Gaussian, (ii) the noise in detectors I and II is uncorrelated, and (iii) the noise spectral density $S_h(f)$ is the same in the two detectors. ''Gaussianity'' means that each Fourier component $\tilde{n}_\alpha(f)$ has
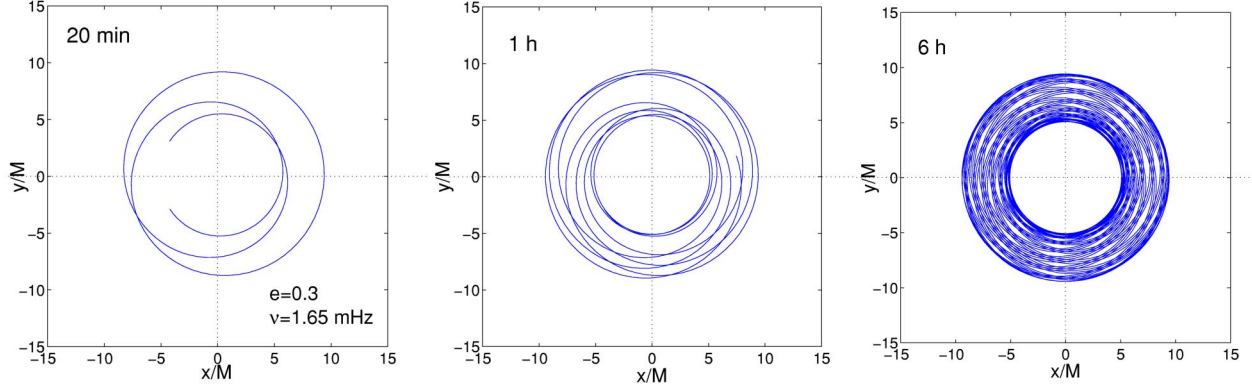
FIG. 3. Same as in Fig. 2, for a trajectory with LSO eccentricity $e=0.3$.

a Gaussian probability distribution. The combination of assumptions (ii) and (iii) is expressed by the relation

$$\langle \tilde{n}_\alpha(f)\tilde{n}_\beta(f')^* \rangle = \frac{1}{2}\delta(f-f')S_n(f)\delta_{\alpha\beta}, \qquad (35)$$

where "$\langle\ \rangle$" denotes the "expectation value" and $S_n(f)$ is the (single-sided) *noise spectral density* for each detector.

Under the assumptions of stationarity and Gaussianity, we have a natural definition of the inner product on the vector space of signals [34]:

$$(\mathbf{p}|\mathbf{q}) \equiv 2\sum_\alpha \int_0^\infty [\tilde{p}_\alpha^*(f)\tilde{q}_\alpha(f) + \tilde{p}_\alpha(f)\tilde{q}_\alpha^*(f)] \Big/ S_n(f)df, \qquad (36)$$

where $p_\alpha(t)$ and $q_\alpha(t)$ are any two signals. One can show, based on this definition, that the inner product of pure noise $\mathbf{n}$ with any signal is a random variable with zero mean and unit variance. In particular, the probability for the noise to have some realization $\mathbf{n}_0$ is just

$$p(\mathbf{n}=\mathbf{n}_0) \propto e^{-(\mathbf{n}_0|\mathbf{n}_0)/2}. \qquad (37)$$

Thus, if the actual incident waveform is $\mathbf{h}$, the probability of measuring a signal $\mathbf{s}$ in the detector output is proportional to $e^{-(\mathbf{s}-\mathbf{h}|\mathbf{s}-\mathbf{h})/2}$. Correspondingly, given a measured signal $\mathbf{s}$, the gravitational waveform $\mathbf{h}$ that "best fits" the data is the one that minimizes the quantity $(\mathbf{s}-\mathbf{h}|\mathbf{s}-\mathbf{h})$.

The SNR for an incident waveform $\mathbf{h}$ filtered by a perfectly matched template $\mathbf{T}=\mathbf{h}$ is

$$\text{SNR}[\mathbf{h}] \equiv \frac{(\mathbf{h}|\mathbf{h})}{\text{rms}(\mathbf{h}|\mathbf{n})}, \qquad (38)$$

where $\text{rms}(\mathbf{h}|\mathbf{n})$ is the rms value for an ensemble of realizations of the detector noise, $\mathbf{n}$. From the definition (36) it follows [34] that for any two signals $p_\alpha(t)$ and $q_\alpha(t)$, the expectation value of $(\mathbf{p}|\mathbf{n})(\mathbf{q}|\mathbf{n})$ is just $(\mathbf{p}|\mathbf{q})$. In particular, we have $\text{rms}(\mathbf{h}|\mathbf{n})=(\mathbf{h}|\mathbf{h})^{1/2}$, and hence the SNR of the detection is approximately given by just

$$\text{SNR}[\mathbf{h}] = (\mathbf{h}|\mathbf{h})^{1/2}. \qquad (39)$$

For a given incident gravitational wave, different realizations of the noise will give rise to somewhat different best-fit parameters. However, for large SNR, the best-fit parameters will have a Gaussian distribution centered on the correct values. Specifically, let $\tilde{\lambda}^a$ be the "true" values of the physical parameters, and let $\tilde{\lambda}^a + \delta\lambda^a$ be the best fit parameters in the presence of some realization of the noise. Then for large SNR, the parameter-estimation errors $\delta\lambda^a$ have the Gaussian probability distribution

$$p(\delta\lambda^a) = \mathcal{N}e^{-(1/2)\Gamma_{ab}\delta\lambda^a\delta\lambda^b}. \qquad (40)$$

Here Γ_{ab} is the so-called *Fisher information matrix*, defined by

$$\Gamma_{ab} \equiv \left(\frac{\partial \mathbf{h}}{\partial \lambda^a} \Big| \frac{\partial \mathbf{h}}{\partial \lambda^b} \right), \qquad (41)$$

and $\mathcal{N}=\sqrt{\det(\Gamma/2\pi)}$ is the appropriate normalization factor. For large SNR, the variance-covariance matrix is given by

$$\langle \delta\lambda^a \delta\lambda^b \rangle = (\Gamma^{-1})^{ab} + \mathcal{O}(\text{SNR})^{-1}. \qquad (42)$$

We define $\Delta\lambda^a \equiv \langle \delta\lambda^a \delta\lambda^a \rangle^{1/2}$ (the repeated index is *not* being summed here). The uncertainty in the source's angular position, $\Delta\Omega_S$ (a solid angle), is given by [10][5]

$$\Delta\Omega_S = 2\pi\sqrt{(\Delta\mu_S\Delta\phi_S)^2 - \langle\delta\mu_S\delta\phi_S\rangle^2}. \qquad (43)$$

The second term in brackets in Eq. (43) accounts for the fact that errors in μ_S and ϕ_S will in general be correlated, so that the "error box" on the sky is elliptical in general, not circular. The 2π factor on the right-hand side (RHS) of Eq. (43) is our convention; with this definition, the probability that the source lies *outside* an (appropriately shaped) error ellipse enclosing solid angle $\Delta\Omega$ is $e^{-\Delta\Omega/\Delta\Omega_S}$. In the same way, the error ellipse for the spin direction, $\Delta\Omega_K$, is given by

$$\Delta\Omega_K = 2\pi\sqrt{(\Delta\mu_K\Delta\phi_K)^2 - \langle\delta\mu_K\delta\phi_K\rangle^2}. \qquad (44)$$

---

[5]Note Eq. (3.7) of [10] is erroneous. However, the results quoted in that paper are based on the correct expression, Eq. (43) here.
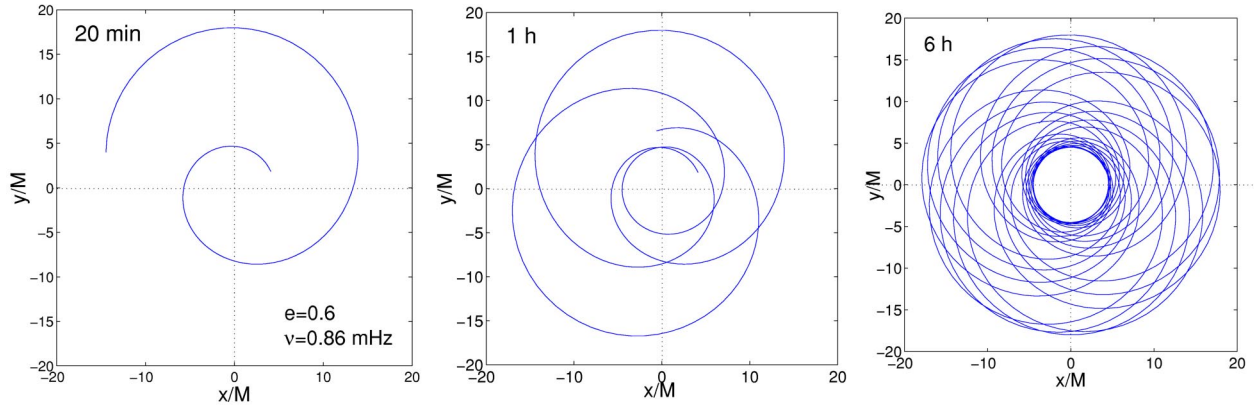
FIG. 4. Same as in Fig. 2, for a trajectory with LSO eccentricity $e = 0.6$.

The actual inner product, Eq. (36), is formulated in the frequency domain. For a white noise [i.e., $S_n(f) = $ const], the inner product is equivalent to $2S_n^{-1}\Sigma_\alpha \int_{-\infty}^{\infty} p_\alpha(t)q_\alpha(t)dt$, by Parseval's theorem. Motivated by this formula, we shall adopt the following approximate version of the inner product in calculating the Fisher matrix: First, we define the "noise-weighted" waveform

$$\hat{h}_\alpha(t) \equiv \sum_n h_{\alpha,n}(t)/S_h^{1/2}(f_n(t)), \qquad (45)$$

where we take

$$f_n(t) = n\nu(t) + \dot{\tilde{\gamma}}(t)/\pi. \qquad (46)$$

Then we approximate the covariance matrix, Eq. (41), as

$$\Gamma_{ab} = 2\sum_\alpha \int_0^T \partial_a \hat{h}_\alpha(t) \partial_b \hat{h}_\alpha(t) dt. \qquad (47)$$

That is, we simply reweight each harmonic by the square root of the inverse spectral density of the noise, and thereafter treat the noise as if it were white.

The decision to set $f_n(t) = n[\nu(t) + (2/n)(\dot{\tilde{\gamma}}(t)/2\pi)]$ is something of a compromise: The radial orbital frequency is ν, the azimuthal orbital frequency is $\nu(t) + (\dot{\tilde{\gamma}}/2\pi)$, and the fully correct waveforms will contain harmonics of both. Our "compromise" approximates the signal as harmonics of $\nu + (2/n)(\dot{\tilde{\gamma}}/2\pi)$, which lies between the radial and azimuthal frequencies[6] and is the "correct" choice for circular motion (in which case the $n = 2$ harmonic dominates the GW output, and only the azimuthal piece enters the waveform).

V. SNR ESTIMATES

Our analysis of the SNR buildup follows, basically, that of Finn and Thorne [16]. The main advance here is, of course, the fact that we consider realistically eccentric orbits, whereas Finn and Thorne confined their analysis to circular

orbits. Unlike in the circular-orbit case, where the contribution from the $n = 2$ harmonic always dominates the SNR, eccentric orbits have their emitted power (and contribution to SNR) distributed among higher n-harmonics. One of the goals of this section is to explore this mode distribution, for realistic values of the orbital eccentricity.

A. LISA noise model

LISA's noise has three components: instrumental noise, confusion noise from short-period galactic binaries, and confusion noise from extragalactic binaries. Our treatment of these three sources follows Hughes [35], though we use somewhat different estimates for the sizes of the three pieces.

For LISA's instrumental noise, $S_h^{inst}(f)$, we use the following analytic fit by Finn and Thorne [16],[7] based on the noise budget given in the LISA Pre-Phase A Report [1]:

$$S_h^{inst}(f) = 1.22 \times 10^{-51} f^{-4} + 2.12 \times 10^{-41}$$
$$+ 1.22 \times 10^{-37} f^2 \text{ Hz}^{-1}, \qquad (48)$$

where the frequency f is to be given in Hz.

Next we turn to WD confusion noise. Any isotropic background of indistinguishable GW sources represents (for the purpose of analyzing *other* sources) a noise source with spectral density [36]

$$S_h^{conf}(f) = \frac{3}{5\pi} f^{-3} \rho_c \Omega_{GW}(f), \qquad (49)$$

where $\rho_c \equiv 3H_0^2/(8\pi)$ is the critical energy density needed to close the universe (assuming it is matter-dominated) and $\Omega_{GW} \equiv (\rho_c)^{-1} d\rho_{GW}/d(\ln f)$ is the energy density in gravitational waves (expressed as a fraction of the closure density)

---

[6]Except for the $n = 1$ harmonic, which, however, contributes very little to the GW signal and to the overall SNR—cf. the plots in Figs. 9–14 below.

[7]To obtain this expression, we used the expression given at the beginning of p. 8 of Ref. [16], where for $[h_{SN5,1\,yr}^{SA}(f)]^2$ we used the expression given in footnote [44] therein, and for Δf we have taken $1/1$ yr.
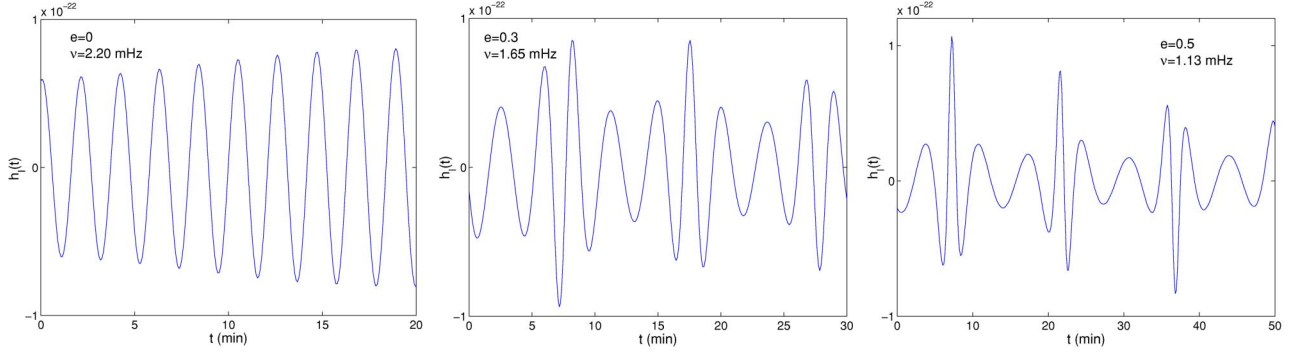
FIG. 5. Sample waveforms. Shown is the response function $h_I(t)$ (as defined in the text) during the last minutes before the final plunge. The three panels show cases with LSO eccentricity 0, 0.3, and 0.5 (left to right, respectively). The other physical parameters are set as follows: CO's mass: $\mu = 10 M_\odot$; MBH's mass: $M = 10^6 M_\odot$; MBH's spin magnitude: $S = M^2$; Angle between MBH's spin and orbital angular momentum: $\lambda = 30°$.

per logarithmic frequency interval.[8] For the extragalactic WD background, Farmer and Phinney [37] estimate that, for f near 1 mHz, $\Omega_{GW}(f) = 3.6 \times 10^{-12} (f/10^{-3} \text{ Hz})^{2/3}$ [at $H_0 = 70 \text{ km}/(\text{sec Mpc})$], so

$$S_h^{\text{ex gal}} = 4.2 \times 10^{-47} \left(\frac{f}{1 \text{ Hz}} \right)^{-7/3} \text{ Hz}^{-1}. \qquad (50)$$

Note Eq. (50) is not a good fit to $S_h^{\text{ex gal}}$ for $f \gtrsim 10^{-2}$ Hz, where mergers cause the spectrum to decrease more sharply. However, at such high frequencies, instrumental noise dominates the total noise in any case, so for our purposes the extrapolation of Eq. (50) to high frequencies is harmless.

A recent calculation of the galactic confusion background by Nelemans *et al.* [38] yields an Ω_{GW}^{gal} that is 5.0×10^1 times larger than $\Omega_{GW}^{\text{ex gal}}$ (near 1 mHz) [37]; therefore[9]

$$S_h^{\text{gal}}(f) = 2.1 \times 10^{-45} \left(\frac{f}{1 \text{ Hz}} \right)^{-7/3} \text{ Hz}^{-1}. \qquad (51)$$

This is larger than instrumental noise in the range $\sim 10^{-4} - 10^{-2}$ Hz. However, at frequencies $f \gtrsim 3 \times 10^{-3}$ Hz, galactic sources are sufficiently sparse, in frequency space, that one expects to be able to "fit them out" of the data. An estimate of the resulting noise is [35]

––––––––––

[8]Note the RHS of our Eq. (49) is a factor $\frac{3}{4}$ as large as the RHS in Eq. (3.4) in [36]; this difference arises simply because the angle between any two LISA arms is $\pi/3$ (instead of the $\pi/2$ for LIGO's arms), and $\sin^2(\pi/3) = 3/4$.

[9]Note our prefactor 2.1×10^{-45} is a factor ~ 25 lower than the prefactor cited in Hughes [35], based on his private communication with S. Phinney. This large discrepancy seems to be the product of the following two factors. First, it was based on the estimate of Ω_{GW}^{gal} by Webbink and Han [39], which is ~ 3 times larger than the result of Nelemans *et al.* [38]. Second, it contained a factor 20/3 error due to a misunderstanding of Phinney's normalization convention.

$$S_h^{\text{inst+gal}}(f) = \min\{S_h^{\text{inst}}(f)/\exp(-\kappa T_{\text{mission}}^{-1} dN/df),$$
$$S_h^{\text{inst}}(f) + S_h^{\text{gal}}(f)\}. \qquad (52)$$

Here dN/df is the number density of galactic white dwarf binaries per unit GW frequency, T_{mission} is the LISA mission lifetime (so $\Delta f = 1/T_{\text{mission}}$ is the bin size of the discretely Fourier transformed data), and κ is the average number of frequency bins that are "lost" (for the purpose of analyzing other sources) when each galactic binary is fitted out (κ is larger than one because LISA's motion effectively smears the signal from each binary over several frequency bins). The factor $\exp(-\kappa T_{\text{mission}}^{-1} dN/df)$ is therefore the fraction of "uncorrupted" bins, where instrumental noise still dominates. For dN/df we adopt the estimate [35]

$$\frac{dN}{df} = 2 \times 10^{-3} \text{ Hz}^{-1} \left(\frac{1 \text{ Hz}}{f} \right)^{11/3}, \qquad (53)$$
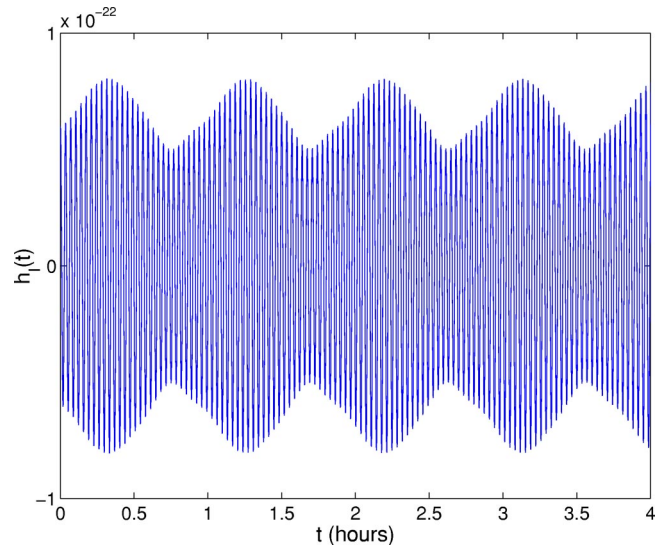

FIG. 6. A longer waveform segment shows amplitude modulations due to precession of the orbital plane. (The physical parameters are set here as in the left panel of Fig. 5.)
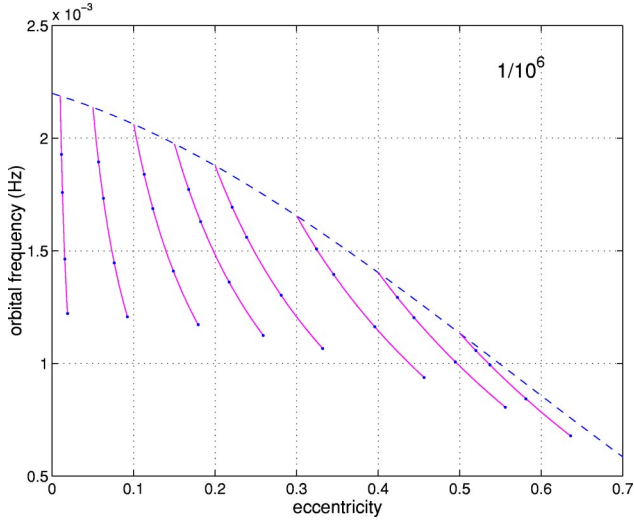
FIG. 7. Evolution of orbits in our model, for a system composed of a $1M_\odot$ CO inspiralling into a $10^6 M_\odot$ (nonspinning) MBH. The dashed line represents the last stable orbit (LSO). Each of the solid lines shows the ν-e trajectory of a system with given initial data (the orbit evolves in time "from bottom to top"). The four dots plotted along each trajectory indicate, from bottom to top, the state of the system 10, 5, 2, and 1 years before the LSO.

and take $\kappa T_{\text{mission}}^{-1}=1.5/\text{yr}$ (corresponding to $T_{\text{mission}}\approx 3$ yr and $\kappa\approx 4.5$ [40]). To obtain the *total* LISA noise, we just add to Eq. (52) the contribution from the extragalatic confusion background, Eq. (50):

$$S_h(f)=S_h^{\text{inst}+\text{gal}}(f)+S_h^{\text{ex gal}}(f). \qquad (54)$$

B. SNR estimates for inspiral orbits

For a Keplerian orbit, the source is strictly periodic and hence the GWs are at harmonics $f_n\equiv n\nu$ of the orbital frequency. However, as discussed in Sec. IV, to partially compensate for the fact that the radial and azimuthal periods are
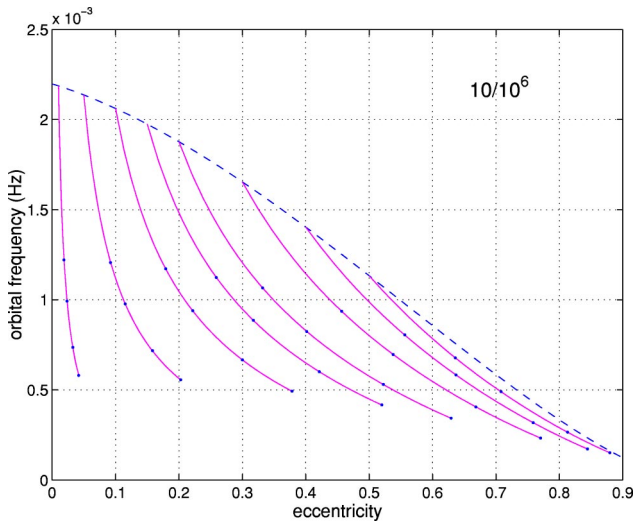

FIG. 8. Same as in Fig. 7, for a $10M_\odot$ CO inspiralling into a $10^6 M_\odot$ MBH.

different, we set $f_n(t)$ equal to $n\nu(t)+\dot{\tilde{\gamma}}(t)/\pi$. Assuming the contributions from the various harmonics to be approximately orthogonal, we may approximate the SNR from a single synthetic 2-arm Michelson detector (denoted here by SNR_I) as

$$\langle\text{SNR}_\text{I}^2\rangle_\text{SA}=\Sigma_n\int\frac{h_{c,n}^2(f_n)}{5f_nS_h(f_n)}d(\ln f), \qquad (55)$$

where "$\langle\dots\rangle_\text{SA}$" means "sky average," i.e., average over all source directions (the factor 5 in the denominator results from this averaging). The *characteristic amplitude* $h_{c,n}$ is given, following Finn and Thorne,[10] by

$$h_{c,n}=(\pi D)^{-1}\sqrt{2\dot{E}_n/\dot{f}_n}, \qquad (56)$$

where $\dot{E}_n$ is the power radiated to infinity by GWs at frequency f_n. To lowest order, this is

$$\dot{E}_n=\frac{32}{5}\mu^2M^{4/3}(2\pi\nu)^{10/3}g(n,e), \qquad (57)$$

where $g(n,e)$ is given by [6]

$$g(n,e)=\frac{n^4}{32}\Bigg\{\Bigg[J_{n-2}(ne)-2eJ_{n-1}(ne)+\frac{2}{n}J_n(ne)$$

$$+2eJ_{n+1}(ne)-J_{n+2}(ne)\Bigg]^2+(1-e^2)[J_{n-2}(ne)$$

$$-2J_n(ne)+J_{n+2}(ne)]^2+\frac{4}{3n^2}[J_n(ne)]^2\Bigg\}. \qquad (58)$$

In this section, our major motivation is to investigate the effect of nonzero eccentricity. For this reason, we ignore the effect of the MBH's spin—effectively assuming the MBH is Schwarzschild.

The curves in Figs. 9–14 show the buildup of SNR with time, for each harmonic. As is customary in the LISA literature, our plots actually give SNR_I—the SNR from a single 2-arm Michelson; the actual LISA SNR buildup will be a factor $\sim\sqrt{2}$ times larger. The curves are derived as follows. We use our PN Eqs. (30) and (28) (with S set to zero) to

---

[10]In their SNR estimates, Finn and Thorne [16] tend to consider the quantity $h'_{c,m}$ (in their notation), the "modified" characteristic amplitude, introduced to account for the reduction in the GW signal near the plunge, where the available bandwidth becomes very small. Here we rather consider $h_{c,m}$ itself: This quantity has the convenient characteristic that when integrated against the frequency [through Eq. (55)] it yields the SNR (squared). An estimate of the SNR based on the plots given in [16], which show the modified amplitudes $h'_{c,m}$ rather than $h_{c,m}$ itself, actually takes into account *twice* the effect of the final plunge: The fact that the frequency changes rapidly near the plunge is already accounted for in the definition of $h_{c,m}$, just above Eq. (2.2) therein.
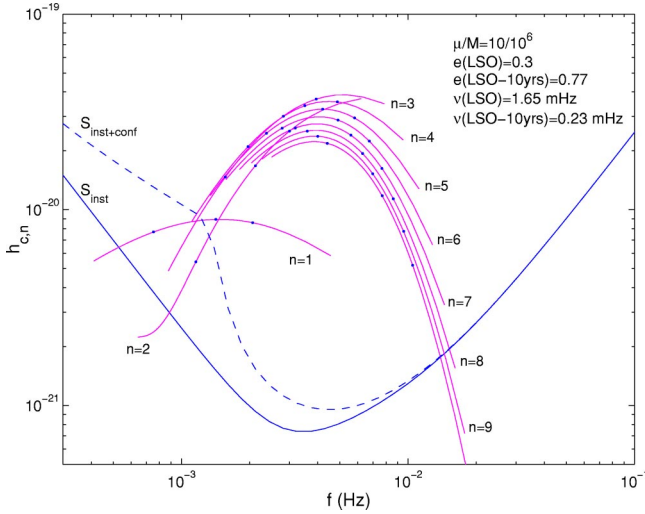
FIG. 9. GW signal from a $10M_\odot$ CO spiralling into a (nonspinning) $10^6M_\odot$ MBH at $D=1$ Gpc: case where eccentricity at the last stable orbit (LSO) is $e_{LSO}=0.3$. The curve labeled "S_{inst}" shows LISA's sky-averaged instrumental noise level, $h_n^{inst}(f)$. The dashed line is an estimate of LISA's overall noise level, $h_n(f)$, including the effect of stochastic-background "confusion" due to WD binaries (both galactic and extra-galactic). The convex curves show the amplitudes $h_{c,n}$ of the first 10 n-harmonics of the GW signal, over the last 10 years of evolution prior to the final plunge. Along each of these curves we marked 3 dots, indicating (from left to right) the GW amplitude 5, 2, and 1 years before the plunge. The orbital eccentricity 10, 5, 2, and 1 years before plunge is 0.77, 0.67, 0.54, and 0.46, respectively. The orbital frequency 10, 5, 2, and 1 years before plunge is 0.23, 0.41, 0.70, and 0.94 mHz, respectively. The frequency at the LSO is 1.65 mHz.

evolve $e(t)$ and $\nu(t)$ forward in time, up to the point when the CO plunges over the top of the effective potential barrier. For a point particle in Schwarzschild, the plunge occurs at $a_{min}=M(6+2e)(1-e^2)^{-1}$ [7], so we set

$$\nu_{max}=(2\pi M)^{-1}[(1-e^2)/(6+2e)]^{3/2}. \qquad (59)$$

We denote by e_f the "final" value of e, i.e., the value of e when ν reaches the plunge frequency ν_{max}. Then, for each harmonic n we use our solution $\{\nu(t),e(t)\}$ along with Eqs. (56), (57), and (58) to determine $h_{c,n}(f_n)$.

The upper "signal" curves in Figs. 9–14 show $h_{c,n}(t)$ for each n; we "cut off" each curve at $f_{n,max}=n\nu_{max}+\pi^{-1}\dot{\tilde{\gamma}}(\nu_{max},e_f)$. Marks along each curve indicate (from right to left) one, two, five, and ten years before the final plunge. The lower "noise" curve depicts $h_n(f)$ $\equiv[5fS_h(f)]^{1/2}$, the rms noise amplitude per logarithmic frequency interval [the factor of 5 comes from sky-averaging; Finn and Thorne [16] define $S_h^{SA}(f)=5S_h(f)$]. For comparison, the instrumental contribution, $h_h^{inst}(f)\equiv[5f_n\times S_h^{inst}(f_n)]^{1/2}$, is also plotted. With these conventions, the contribution to the SNR from each harmonic is

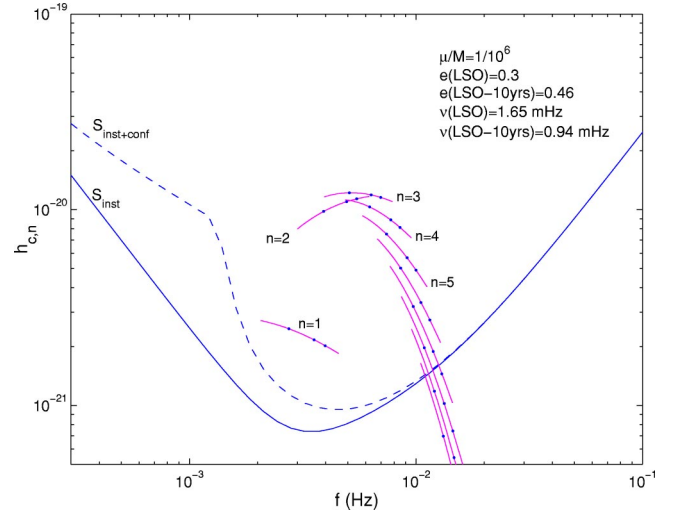$$(\text{SNR}_I)_n^2=\int (h_{c,n}/h_n)^2 d(\ln f), \qquad (60)$$

FIG. 10. Same as in Fig. 9, but for inspiral of a $1M_\odot$ CO into a $10^6M_\odot$ MBH. The orbital eccentricity 10, 5, 2, and 1 years before plunge is 0.46, 0.40, 0.35, and 0.32, respectively. The orbital frequency ν 10, 5, 2, and 1 years before plunge is 0.94, 1.16, 1.39, and 1.51 mHz, respectively. The frequency at the LSO is 1.65 mHz.

so using the curves one can "integrate by eye" to estimate the contribution to the SNR from each harmonic, and to detect *when* (i.e., how long before the final plunge) most of the contribution is accumulated.

Here are some points to pay attention to when examining the SNR plots in Figs. 9–14:

Systems with MBH's mass of $\sim 10^6$ are ideally "located" in the LISA band. Systems with $M=10^7$ radiate at frequencies where WD confusion noise would likely obscure the capture signal.

Systems with $M\approx 10^6$ at $D=1$ Gpc are detectable with SNR_I of $\sim 5(\mu/1M_\odot)$, assuming 1 year of signal integration.
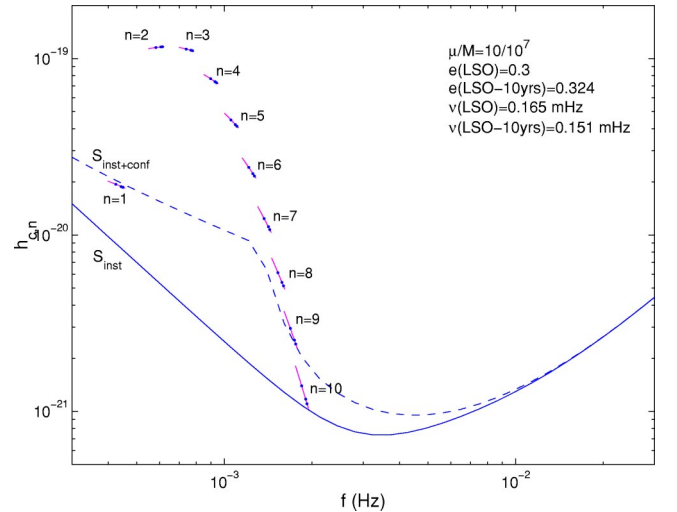

FIG. 11. Same as in Fig. 9, but for inspiral of a $10M_\odot$ CO into a $10^7M_\odot$ MBH. The orbital eccentricity 10, 5, 2, and 1 years before plunge is 0.324, 0.313, 0.305, and 0.303, respectively. The orbital frequency 10, 5, 2, and 1 years before plunge is 0.151, 0.158, 0.162, and 0.164 mHz, respectively. The frequency at the LSO is 0.165 mHz.
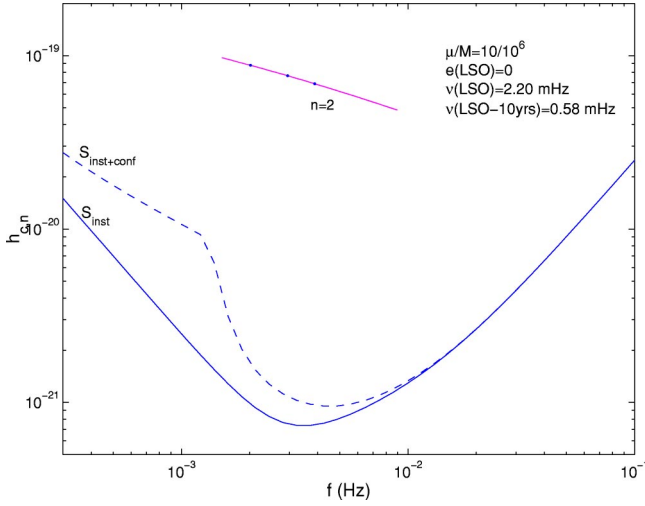
FIG. 12. GW signal from a $10M_\odot$ CO spiralling into a (non-spinning) $10^6 M_\odot$ MBH: case of a circular orbit (compare with Fig. 4 of Finn and Thorne). Notation is the same as in Fig. 9. Note that in our model, a CO in a circular orbit emits GW only into the $n=2$ harmonic. The orbital frequency 10, 5, 2, and 1 years before plunge is 0.58, 0.74, 0.99, and 1.22 mHz, respectively. The frequency at the LSO is 2.20 mHz.

Combining both synthetic Michelsons, and for two years of integration, LISA's SNR is $\sim 10(\mu/1M_\odot)$.

As expected, the higher the orbital eccentricity, the more SNR is contributed by high n-harmonics. At $e_{\rm LSO}=0.3$, the contribution from $n=3,4$ is equally important to that of $n=2$. At $e_{\rm LSO}=0.5$, the dominant contribution comes at $n=4$, and one needs to sum the contributions of at least a dozen modes in order to properly estimate the overall SNR.

A related point: For $10^6 M_\odot$ MBHs and $\sim 1M_\odot$ COs, the last year prior to plunge contributes only a small fraction of the potential SNR. Even for $\sim 10M_\odot$ COs, the contribution
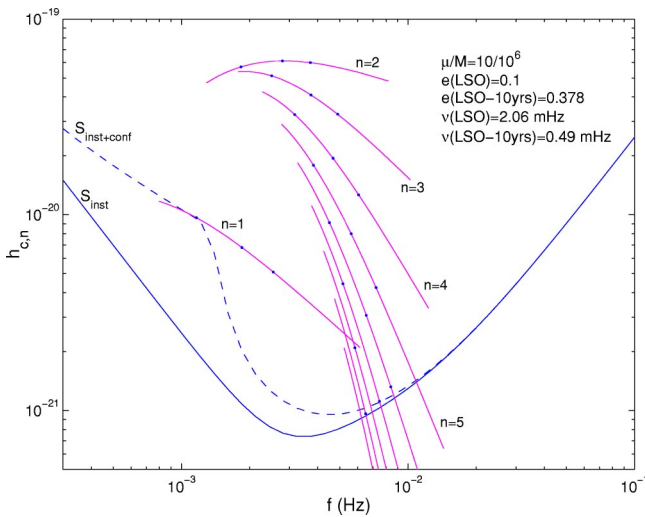

FIG. 13. Same as in Fig. 9, except that the LSO eccentricity is taken to be 0.1. The orbital eccentricity 10, 5, 2, and 1 years before plunge is 0.38, 0.30, 0.22, and 0.18, respectively. The orbital frequency 10, 5, 2, and 1 years before plunge is 0.49, 0.67, 0.94, and 1.17 mHz, respectively. The frequency at the LSO is 2.06 mHz.
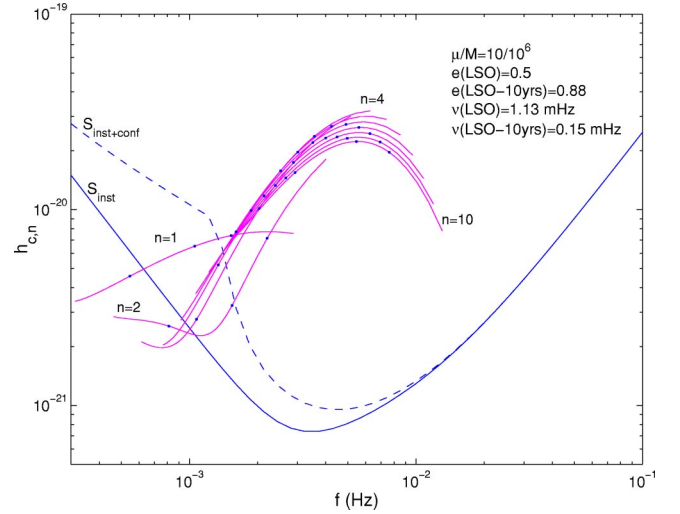

FIG. 14. GW signal from a $10M_\odot$ CO spiralling into a $10^6 M_\odot$ MBH: case where eccentricity at the last stable orbit is $e_{\rm LSO}=0.5$. Notation is the same as in Fig. 9. The orbital eccentricity 10, 5, 2, and 1 years before plunge is 0.88, 0.81, 0.71, and 0.64, respectively. The orbital frequency 10, 5, 2, and 1 years before plunge is 0.151, 0.265, 0.490, and 0.678 mHz, respectively. The frequency at the LSO is 1.13 mHz.

between 10 and 1 years prior to plunge can easily exceed the contribution from the last year.

The last effect may be further visualized by looking at the total amount of energy radiated in GW up to a time t prior to plunge, as a function of t. This is demonstrated in Fig. 15 for a mass ratio of $(10M_\odot)/(10^6 M_\odot)$ and for a variety of LSO eccentricities. For this plot, we used the leading-order expression given in [6] for the total power radiated from all n-harmonics:

$$\dot{E}(t) = \frac{32}{5}(\mu/M)^2[2\pi\nu(t)M]^{10/3}[1-e(t)^2]^{-7/2}$$

$$\times [1+(73/24)e^2(t)+(37/96)e^4(t)]. \quad (61)$$

The percentage of energy radiated up to time t, out of the total energy radiated during the capture, is then calculated through

$$\%E_{\rm rad}(t) = \left(1 - \frac{\int_t^{t_{\rm LSO}} \dot{E}(t')dt'}{\int_{-\infty}^{t_{\rm LSO}} \dot{E}(t')dt'}\right) \times 100. \quad (62)$$

The results are striking: For a $10^6 M_\odot$ MBH and a $10M_\odot$ CO, about half the total GW energy is released earlier than 10 years before the final plunge; for a $1M_\odot$ CO, half the energy is emitted already 100 years before plunge. Most of this energy is released in the LISA band, in short "spurts" as the CO passes close to the MBH. This provides a vivid demonstration of the potential "threat" imposed by self-confusion. A systematic analysis of this issue will be presented elsewhere.
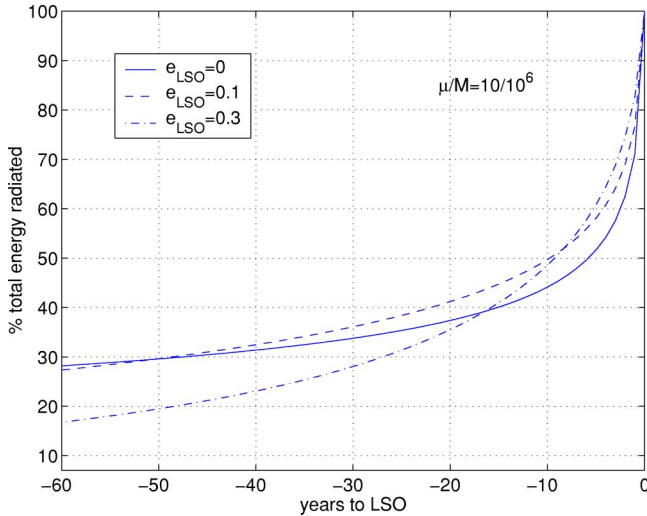
FIG. 15. Percentage of energy radiated (out of the total energy radiated in GW to infinity during the entire capture process) as a function of the time left to the final plunge. The CO and MBH masses are $10M_\odot$ and $10^6 M_\odot$, respectively. This plot was generated using Eq. (62) with $\dot{E}$ approximated using Eq. (61). Note how large the time scale is for energy to be emitted in GW by the CO-MBH system, compared to LISA mission time (~ 2 years).

Finally, recall that all of our results regarding SNR values should be regarded as ballpark estimates rather than definite, due to the many approximations made here. Here is a summary of the various approximations involved: (i) we incorporate an approximate model of LISA's instrumental noise, which is inaccurate at the high-frequency end; (ii) we model the source using PN evolution and quadrupole emission—both approximations being worse, again, at high frequencies; (iii) we assume a nonrotating MBH; (iv) we assume the contributions from the various n-modes to the SNR are uncoupled; and (v) we assume that an ideal, coherent matched filtering search is carried out over the entire observation period. Nevertheless, we believe our results amply illustrate the importance of higher harmonics and of searches with multi-year integration times.

C. SNR for a low-mass main-sequence star at Sgr A*

Freitag [18,41] recently pointed out that LISA might be able to detect a few $\sim 0.1 M_\odot$ main-sequence stars captured by the MBH at the center of our own galaxy. The strongest such source will still have $\sim 10^6$ years to go before plunge, and so will currently be at the low end of the LISA frequency range, but because it is so close to us, Freitag estimated that it could still yield a SNR_I as high as ~ 100. We have re-examined this estimate, using the example from Fig. 1 in Freitag [41], in which $\mu = 0.06 M_\odot$, $M = 2.6 \times 10^6 M_\odot$, $D = 8$ kpc, and $e = 0.8$ at ten million years prior to plunge. The results are shown in Fig. 16. Since for the galactic source considered here, there is practically no frequency evolution during the observation time, our convention in Fig. 16 differs somewhat from those in Figs. 9–14. As in Figs. 9–14, the different curves correspond to the contributions from different harmonics, but here we plot $h_{c,n}$ times the factor
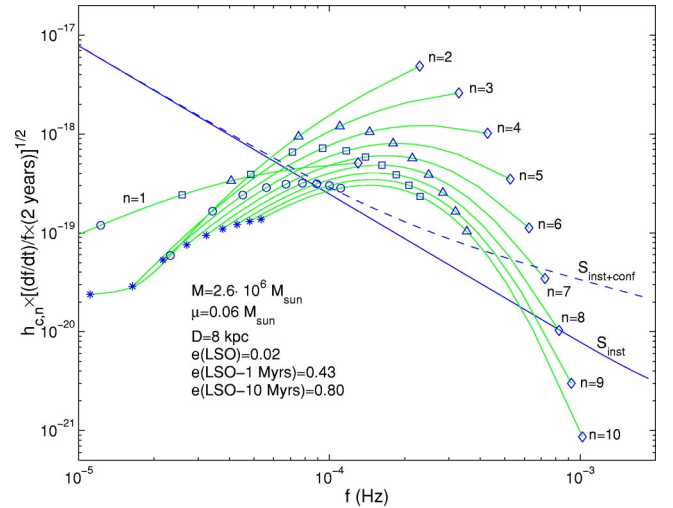

FIG. 16. SNR for a low-mass main-sequence star at Sgr A*. $\diamond$ indicates the SNR accumulated over 2 years of observation when the system is 10^5 years before plunge. $\triangle$, $\square$, $\bigcirc$, and $*$ similarly correspond to 10^6, 2×10^6, 5×10^6, and 10^7 years before plunge, respectively.

$[(f_n^{-1} df_n/dt) \times 2 \text{ yr}]$, so the height of the marked point above the noise curve now gives SNR accumulated over 2 years of observation. The marked points correspond to 2-yr observations carried out 10^7, 5×10^6, 2×10^6, 10^6, and 10^5 years before plunge, respectively. (Actually, there is no "plunge," as the low-mass star is tidally disrupted at least ~ 50 yrs before plunge would occur, but we can ignore that for this analysis.)

For a signal coming 10^6 years before plunge, we find a 2-yr SNR_I of ~ 11 (the square root of the sum of the squares of the contributions from all modes). A two-year observation only 10^5 years before plunge would yield $\text{SNR}_\text{I} \approx 55$. These SNR_I values are a factor ~ 4 times smaller than the values obtainable from Fig. 1 of Freitag [41] (when the 1-yr results he gives there are scaled up to two years), but still support the idea that this is a potentially observable source. As Freitag points out [41], tidal heating could possibly (under pessimistic assumptions) disrupt the low-mass star sometime between 10^6 and 10^5 years prior to plunge, so the higher SNR_I value must be treated with some caution.

VI. PARAMETER ESTIMATION

A. Numerical implementation

For our parameter-accuracy estimates we wrote a simple numerical code, based on the following prescription.

Pick a specific point λ^a in parameter space. We found it convenient to first prescribe a value for the eccentricity at the LSO, e_LSO; then get the associated LSO frequency using, for simplicity, the Schwarzschild value [7]

$$\nu_\text{LSO} = (2\pi M)^{-1}[(1 - e_\text{LSO}^2)/(6 + 2e_\text{LSO})]^{3/2}; \quad (63)$$

and finally obtain e_0 and ν_0 by integrating the evolution equations of Sec. III F one year back in time. The parameter

TABLE II. Parameter accuracy estimates for inspiral of a $1 M_\odot$ CO onto a $10^6 M_\odot$ MBH at SNR=30 (based on data collected during the last year of inspiral). Shown are results for various values of the MBH's spin magnitude S and the final eccentricity e_{LSO}. The rest of the parameters are set as follows: $t_0 = t_{LSO} - (1/2)$ yr (middle of integration), $\tilde{\gamma}_0 = 0$, $\Phi_0 = 0$, $\theta_S = \pi/4$, $\phi_S = 0$, $\lambda = \pi/6$, $\alpha_0 = 0$, $\theta_K = \pi/8$, and $\phi_K = 0$.

S/M^2	0.1	0.1	0.1	0.5	0.5	0.5	1	1	1	1
e_{LSO}	0.1	0.3	0.5	0.1	0.3	0.5	0.1	0.3	0.4	0.5
$\Delta(\ln M)$	2.3×10^{-3}	1.1×10^{-3}	2.0×10^{-3}	6.9×10^{-4}	1.3×10^{-3}	1.8×10^{-3}	9.2×10^{-4}	1.3×10^{-3}	2.0×10^{-3}	6.5×10^{-3}
$\Delta(S/M^2)$	2.5×10^{-4}	1.3×10^{-4}	3.0×10^{-4}	3.6×10^{-4}	8.5×10^{-4}	1.7×10^{-3}	1.0×10^{-3}	2.1×10^{-3}	6.3×10^{-3}	1.3×10^{-2}
$\Delta(\ln \mu)$	1.0×10^{-3}	3.2×10^{-4}	1.7×10^{-3}	3.9×10^{-4}	2.2×10^{-4}	4.0×10^{-3}	3.4×10^{-4}	6.0×10^{-4}	7.4×10^{-3}	5.4×10^{-2}
$\Delta(e_0)$	7.1×10^{-4}	2.7×10^{-4}	5.0×10^{-4}	7.6×10^{-4}	4.4×10^{-4}	8.2×10^{-4}	1.2×10^{-3}	8.6×10^{-4}	3.0×10^{-3}	9.7×10^{-3}
$\Delta(\cos \lambda)$	6.2×10^{-2}	3.1×10^{-2}	6.5×10^{-2}	3.6×10^{-3}	7.9×10^{-3}	1.4×10^{-2}	2.5×10^{-3}	4.8×10^{-3}	1.3×10^{-2}	2.3×10^{-2}
$\Delta(\Omega_s)$	1.3×10^{-3}	9.4×10^{-4}	3.4×10^{-4}	1.4×10^{-3}	9.8×10^{-4}	3.7×10^{-4}	1.6×10^{-3}	9.4×10^{-4}	7.8×10^{-4}	4.2×10^{-4}
$\Delta(\Omega_K)$	5.9×10^{-2}	6.4×10^{-2}	8.7×10^{-2}	5.4×10^{-2}	5.1×10^{-2}	4.9×10^{-2}	5.3×10^{-2}	5.0×10^{-2}	5.1×10^{-2}	5.3×10^{-2}
$\Delta(\tilde{\gamma}_0)$	5.6×10^{-1}	9.7×10^{-1}	3.1×10^{-1}	5.4×10^{-1}	8.9×10^{-1}	3.1×10^{-1}	$4.6\times10^{+0}$	3.5×10^{-1}	5.1×10^{-1}	3.8×10^{-1}
$\Delta(\Phi_0)$	4.1×10^{-1}	8.8×10^{-1}	7.9×10^{-2}	4.2×10^{-1}	9.3×10^{-1}	8.1×10^{-2}	$5.8\times10^{+0}$	1.8×10^{-1}	5.6×10^{-1}	3.0×10^{-1}
$\Delta(\alpha_0)$	6.2×10^{-1}	5.7×10^{-1}	5.4×10^{-1}	6.2×10^{-1}	5.8×10^{-1}	5.5×10^{-1}	9.7×10^{-1}	5.9×10^{-1}	5.7×10^{-1}	5.6×10^{-1}
$\Delta[\ln(\mu/D)]$	2.2×10^{-1}	4.0×10^{-2}	7.1×10^{-2}	2.2×10^{-1}	3.8×10^{-2}	6.4×10^{-2}	3.7×10^{-2}	8.2×10^{-2}	3.9×10^{-2}	4.2×10^{-2}
$\Delta(t_0)\nu_0$	8.0×10^{-2}	1.5×10^{-1}	1.4×10^{-2}	8.4×10^{-2}	1.6×10^{-1}	1.5×10^{-2}	$1.0\times10^{+0}$	3.6×10^{-2}	9.5×10^{-2}	4.8×10^{-2}

t_0 is set to be in the middle of the integration time. Namely, the integration is carried out from $t_{init} \equiv t_0 - (1/2)$ yr to $t_{LSO} \equiv t_0 + (1/2)$ yr.

For that point, calculate the n-modes $h_{I,n}(t)$ and $h_{II,n}(t)$ of Eq. (14), for the last year of inspiral, as described in Sec. III. The number of modes one has to take into account varies with the prescribed LSO eccentricity. We determined this number by requiring that the relative error in the final Fisher matrix components due to omission of higher-n modes is not greater than $\sim 10^{-6}$. At $e_{LSO} = 0.5$ this meant summing over ~ 20 modes. Note that at the n'th mode, the 1-year long function $h_{\alpha,n}$ contains a huge number of wave cycles—roughly $\sim 10^5 n$. The time resolution has been set such that each wave cycle is sampled at least 10 times. At $n = 20$, this meant a time resolution of about 5 seconds.

For each relevant n, use Eq. (54) to calculate LISA'a noise $S_n(f_n)$. Then sum over modes using Eq. (45) to obtain the "noise-weighted" waveforms $\hat{h}_I(t)$ and $\hat{h}_{II}(t)$.

Calculate the SNR through Eq. (39), using the time-domain approximation for the inner product:

$$\text{SNR}^2 = 2 \sum_{\alpha=I,II} \int_{t_{init}}^{t_{LSO}} \hat{h}_\alpha^2(t) dt. \tag{64}$$

Calculate the 13×2 derivatives $\partial_a \hat{h}_\alpha \equiv \partial \hat{h}_\alpha / \partial \lambda^a$. We take these derivatives numerically, through $[\hat{h}_\alpha(\lambda^a \to \lambda^a + \delta\lambda^a/2) - \hat{h}_\alpha(\lambda^a \to \lambda^a - \delta\lambda^a/2)] / \delta\lambda^a$ (for each $\lambda^a = \lambda^0, \ldots, \lambda^{13}$). Namely, for each derivative we calculate the waveform twice, with the relevant parameter shifted by $\pm \delta\lambda^a/2$. The shift $\delta\lambda^a$ is set such that the resulting relative error in the Fisher-matrix elements is $\lesssim 10^{-6}$. [The dependence of the waveform in some of the parameters is such the derivatives can, in principle, be taken analytically. For some other parameters (like e_0 or Φ_0) the dependence is less ex-

plicit, and one is required to take the derivatives numerically. We found it convenient (and accurate enough) to take all derivatives numerically.]

Calculate all elements of the Fisher matrix Γ_{ab}, using Eq. (47).

Use Eq. (42) to calculate the measurement error for each of the parameters:

$$\Delta\lambda^a = \sqrt{(\Gamma^{-1})^{aa}} \tag{65}$$

(no summation over a on the RHS). Obtain $\Delta\Omega_S$ and $\Delta\Omega_K$ using Eqs. (43) and (44). To invert the Fisher matrix, we used a numerical subroutine based on *dgaussj*() of Ref. [42].

Finally, multiply each of the various $\Delta\lambda^a$ by SNR/30. This, in effect, normalizes the distance to the source such that the SNR becomes 30 (roughly the SNR output from a $3 M_\odot$ CO captured by a $10^6 M_\odot$ at $D = 1$ Gpc).

B. Results for 1-yr integrations

Although in Sec. V we stressed the importance of the signal-to-noise built up in the last several years prior to plunge, in this section, due to limitations of computer memory and speed, we restrict ourselves to waveforms coming from the last year of inspiral. In essence, in this section we pretend that LISA is "off-line" prior to $t_{LSO} - 1$ yr, where t_{LSO} is the instant of plunge.

We present our results from inverting the Fisher matrix for MBH mass of $10^6 M_\odot$, CO masses of $1 M_\odot$ and $10 M_\odot$, and a range of values of the MBH spin and the orbital eccentricity at the LSO. The rest of the parameters have been set as follows: $t_0 = t_{LSO} - (1/2)$ yr (middle of integration), $\tilde{\gamma}_0 = 0$, $\Phi_0 = 0$, $\theta_S = \pi/4$, $\phi_S = 0$, $\lambda = \pi/6$, $\alpha_0 = 0$, $\theta_K = \pi/8$, and $\phi_K = 0$. Again, the angles $\bar{\phi}_0$ and $\bar{\alpha}_0$ specifying LISA's position and orientation at t_0 are set to zero. Tables II and III give the results. We expect that the measurement

TABLE III. Parameter extraction accuracy for inspiral of a $10 M_\odot$ CO onto a $10^6 M_\odot$ MBH at SNR$=30$ (based on data collected during the last year of inspiral). Shown are results for various values of the MBH's spin magnitude S and the final eccentricity e_{LSO}. The rest of the parameters are set as follows: $t_0 = t_{\text{LSO}} - (1/2)$ yr (middle of integration), $\tilde{\gamma}_0 = 0$, $\Phi_0 = 0$, $\theta_S = \pi/4$, $\phi_S = 0$, $\lambda = \pi/6$, $\alpha_0 = 0$, $\theta_K = \pi/8$, and $\phi_K = 0$.

S/M^2	0.1	0.1	0.1	0.5	0.5	0.5	1	1	1
e_{LSO}	0.1	0.3	0.5	0.1	0.3	0.5	0.1	0.3	0.5
$\Delta(\ln M)$	2.6×10^{-4}	5.6×10^{-4}	5.3×10^{-5}	2.7×10^{-4}	9.2×10^{-4}	7.7×10^{-5}	2.8×10^{-4}	2.5×10^{-4}	1.5×10^{-4}
$\Delta(S/M^2)$	3.6×10^{-5}	7.9×10^{-5}	4.5×10^{-5}	1.3×10^{-4}	6.3×10^{-4}	5.1×10^{-5}	2.6×10^{-4}	3.7×10^{-4}	2.6×10^{-4}
$\Delta(\ln\mu)$	6.8×10^{-5}	1.5×10^{-4}	7.4×10^{-5}	6.8×10^{-5}	9.2×10^{-5}	1.0×10^{-4}	6.1×10^{-5}	9.1×10^{-5}	1.0×10^{-3}
$\Delta(e_0)$	6.3×10^{-5}	1.3×10^{-4}	2.9×10^{-5}	8.5×10^{-5}	2.8×10^{-4}	3.2×10^{-5}	1.2×10^{-4}	1.1×10^{-4}	1.6×10^{-4}
$\Delta(\cos\lambda)$	6.0×10^{-3}	1.7×10^{-2}	1.3×10^{-3}	1.3×10^{-3}	5.8×10^{-3}	2.4×10^{-4}	6.5×10^{-4}	8.4×10^{-4}	4.7×10^{-4}
$\Delta(\Omega_s)$	1.8×10^{-3}	1.7×10^{-3}	7.9×10^{-4}	2.0×10^{-3}	1.7×10^{-3}	7.6×10^{-4}	2.1×10^{-3}	1.1×10^{-3}	6.7×10^{-4}
$\Delta(\Omega_K)$	5.6×10^{-2}	5.3×10^{-2}	4.7×10^{-2}	5.5×10^{-2}	5.1×10^{-2}	4.7×10^{-2}	5.6×10^{-2}	5.1×10^{-2}	4.8×10^{-2}
$\Delta(\tilde{\gamma}_0)$	4.0×10^{-1}	6.3×10^{-1}	3.8×10^{-1}	$1.0\times10^{+0}$	6.1×10^{-1}	3.9×10^{-1}	9.3×10^{-1}	3.4×10^{-1}	3.9×10^{-1}
$\Delta(\Phi_0)$	2.6×10^{-1}	6.7×10^{-1}	2.2×10^{-1}	$1.4\times10^{+0}$	7.5×10^{-1}	2.7×10^{-1}	$1.5\times10^{+0}$	1.7×10^{-1}	3.3×10^{-1}
$\Delta(\alpha_0)$	6.2×10^{-1}	5.8×10^{-1}	5.5×10^{-1}	6.3×10^{-1}	5.9×10^{-1}	5.6×10^{-1}	6.4×10^{-1}	5.9×10^{-1}	5.9×10^{-1}
$\Delta[\ln(\mu/D)]$	8.7×10^{-2}	3.8×10^{-2}	3.7×10^{-2}	3.8×10^{-2}	3.7×10^{-2}	3.7×10^{-2}	3.8×10^{-2}	7.0×10^{-2}	3.7×10^{-2}
$\Delta(t_0)\nu_0$	4.5×10^{-2}	1.1×10^{-1}	3.3×10^{-2}	2.3×10^{-1}	1.3×10^{-1}	4.4×10^{-2}	2.5×10^{-1}	3.2×10^{-2}	5.5×10^{-2}

accuracies for intrinsic parameters will not depend very sensitively on the source's position and orientation, but that the measurement accuracies for extrinsic parameters (e.g., LISA's angular resolution) will depend rather more sensitively on the actual values of these angles. (This was found to be the case in LISA measurements of MBH-MBH coalescences [21], and we have also been able to verify it, to a limited extent, in the LISA capture case.)

Summarizing the results in Table III, for the case of a $10 M_\odot$ BH spiraling into a $10^6 M_\odot$ MBH, the measurement accuracies for the seven intrinsic parameters are (very roughly) $\Delta(\ln M)\sim 2\times10^{-4}$, $\Delta(\ln\mu)\sim10^{-4}$, $\Delta(S/M^2) \sim10^{-4}$, $\Delta(\cos\lambda)\sim10^{-3}$, $\Delta e_0\sim10^{-4}$, and $\Delta\Phi_0\sim\Delta\tilde{\gamma}_0 \sim0.5$.

Comparing Tables II and III ($1 M_\odot$ vs $10 M_\odot$ CO), we see $\Delta(\ln M)$, $\Delta(\ln\mu)$, $\Delta(S/M^2)$, $\Delta(\cos\lambda)$, and Δe_0 are all typically about an order of magnitude smaller for the $10 M_\odot$ CO case (again, for fixed SNR and fixed 1-yr integration time). This general trend of better accuracy for higher CO mass is not hard to understand. First, since $\dot{\nu}\propto\mu$, it is clear that $\Gamma_{\ln\mu\ln\mu}$ should scale roughly like μ^2, so $\Delta(\ln\mu) \equiv[(\Gamma^{-1})^{\ln\mu\ln\mu}]^{1/2}$ should scale roughly as μ^{-1}. Similarly, the derivative $\partial_{\ln M}h_\alpha(t)$ has size of order $h_\alpha(t)\partial_{\ln M}\Phi(t)$ (during most of the integration time), and it is clear from Eqs. (27), (28) that the typical size of $\partial_{\ln M}\Phi(t)$ scales roughly like μ. The magnitudes of $\partial_{S/M^2}h_\alpha(t)$, $\partial_{\cos\lambda}h_\alpha(t)$, and $\partial_{e_0}h_\alpha(t)$ also scale roughly linearly with μ, for the same reason. Hence, it is reasonable to expect that errors in these five intrinsic variables should scale roughly like μ^{-1}.

We next turn to the extrinsic parameters. Our few examples suggest that LISA's angular resolution for capture sources is $\Delta\Omega_s\sim10^{-3}$ radians, while the MBH spin direction can be determined to within $\Delta\Omega_K\sim5\times10^{-2}$. We find $\Delta[\ln(\mu/D)]\sim5\times10^{-2}$, typically. Since $\Delta(\ln\mu) \ll\Delta[\ln(\mu/D)]$, it is clear that $\Delta(\ln D)\sim5\times10^{-2}$ too. (We may

verify the last statement by examining the $[\ln\mu,\ln(\mu/D)]$ minor of Γ^{-1}: We have

$$(\Gamma^{-1})^{\ln D,\ln D}=(\Gamma^{-1})^{\ln(\mu/D),\ln(\mu/D)}+(\Gamma^{-1})^{\ln\mu,\ln\mu}$$
$$-2(\Gamma^{-1})^{\ln\mu,\ln(\mu/D)},$$

and since typical values are $(\Gamma^{-1})^{\ln(\mu/D),\ln(\mu/D)}\sim10^{-4}$, $(\Gamma^{-1})^{\ln\mu,\ln\mu}\sim10^{-9}$, and $(\Gamma^{-1})^{\ln\mu,\ln(\mu/D)}\sim10^{-9}$, we find that indeed $\Delta(\ln D)\approx\Delta[\ln(\mu/D)]$.) Finally, as a check, it is easy to see that $\Delta[\ln(\mu/D)]$ must be greater than SNR$^{-1}=0.033$ (since the signal amplitude is linear in μ/D), which is indeed satisfied in every column of our tables.

C. Comparison with other results in the literature

Our angular resolution results can be compared to results by Cutler and Vecchio [43] on LISA's angular resolution for monochromatic sources. For a monochromatic source with $f_{gw}=3$ mHz and SNR$=30$, LISA's angular resolution is typically $\Delta\Omega_s\sim5\times10^{-4}$ (estimated by interpolating between Figs. 2 and 3 in [43], after rescaling those figures to SNR$=30$), which is only a factor ~2 smaller than our result for capture sources. Since capture sources have twice as many unknown parameters as monochromatic sources (14 versus 7), it is clear that LISA's angular resolution must be worse for the former (at the same SNR), but the "good news" is that this degradation appears to be quite modest, based on our limited sample.

Our results on the mass and spin determination accuracy can be compared to previous results by Ryan [2] and Poisson [22]. Ryan's waveforms are based on PN evolution equations (similar to ours), while Poisson's are based on a Taylor expansion of the waveform phase near plunge, with expansion coefficients obtained from numerical solution of the Teukolsky equation. Both these authors consider only circular, equatorial orbits (so $e_0=0$ and $\cos\lambda=1.0$, *a priori*). Both

TABLE IV. Parameter extraction accuracy for a low-mass main-sequence star at Sgr A*. We assume $M = 2.6 \times 10^6 M_\odot$, $\mu = 0.06 M_\odot$, and data integration lasting *2 years*. We also assume the star is observed a million years before the (theoretical) plunge, just before tidal effects become important. Each column of the table refers to a different choice of the MBH's spin, orbital eccentricity e and frequency ν at the time of observation. The other parameters are set as follows: $\tilde{\gamma}_0 = 0$, $\Phi_0 = 0$, $\theta_S = 1.66749$ (true value for Sgr A*), $\phi_S = 0$, $\lambda = \pi/6$, $\alpha_0 = 0$, $\theta_K = \pi/8$, and $\phi_K = 0$. Most of the values given in the table result from inverting the full, (14×14)D Fisher matrix. The values for $\Delta \Omega_K$ obtained by inverting the 11×11 minor that excludes the CO's mass μ and the two sky-location coordinates θ_S and ϕ_S (whose precise values are known for Sgr A*) are given in parentheses. (For all other parameters, using the known sky position did not significantly improve measurement accuracy.)

S/M^2	0.1	0.1	0.1	0.5	0.5	0.5	1	1	1
e	0.10	0.43	0.80	0.10	0.43	0.80	0.10	0.43	0.80
ν_0(mHz)	0.044	0.035	0.013	0.044	0.035	0.013	0.044	0.035	0.013
SNR	19.8	29.9	26.4	19.0	28.3	25.7	18.8	28.4	29.7
$\Delta(\ln M)$	3.7×10^{-3}	3.6×10^{-2}	2.1×10^{-1}	5.9×10^{-3}	3.8×10^{-2}	2.1×10^{-1}	1.0×10^{-2}	3.8×10^{-2}	2.1×10^{-1}
$\Delta(S/M^2)$	2.5×10^{-3}	1.9×10^{-3}	6.9×10^{-3}	3.2×10^{-3}	2.5×10^{-3}	5.1×10^{-3}	9.6×10^{-3}	6.8×10^{-3}	9.9×10^{-3}
$\Delta(\ln \mu)$	$6.1 \times 10^{+3}$	$4.0 \times 10^{+3}$	$4.5 \times 10^{+3}$	$6.4 \times 10^{+3}$	$4.3 \times 10^{+3}$	$4.6 \times 10^{+3}$	$6.5 \times 10^{+3}$	$4.2 \times 10^{+3}$	$4.1 \times 10^{+3}$
$\Delta(e_0)$	1.2×10^{-2}	2.4×10^{-2}	3.3×10^{-2}	1.3×10^{-2}	2.5×10^{-2}	3.3×10^{-2}	1.3×10^{-2}	2.5×10^{-2}	3.2×10^{-2}
$\Delta(\cos \lambda)$	3.2×10^{-2}	1.8×10^{-2}	2.0×10^{-2}	2.6×10^{-2}	1.7×10^{-2}	1.8×10^{-2}	2.6×10^{-2}	1.7×10^{-2}	1.6×10^{-2}
$\Delta(\Omega_s)$	3.1×10^{-2}	9.4×10^{-3}	1.1×10^{-2}	2.0×10^{-2}	7.6×10^{-3}	7.0×10^{-3}	2.0×10^{-2}	7.9×10^{-3}	7.1×10^{-3}
$\Delta(\Omega_K)$	3.1×10^{-2}	1.1×10^{-2}	1.0×10^{-2}	1.9×10^{-2}	7.5×10^{-3}	6.2×10^{-3}	2.0×10^{-2}	8.0×10^{-3}	7.5×10^{-3}
	(1.1×10^{-2})	(5.1×10^{-3})	(6.4×10^{-3})	(1.2×10^{-2})	(4.6×10^{-3})	(4.2×10^{-3})	(1.2×10^{-2})	(4.9×10^{-3})	(4.8×10^{-3})
$\Delta(\tilde{\gamma}_0)$	$1.6 \times 10^{+1}$	3.6×10^{-1}	2.5×10^{-1}	$1.5 \times 10^{+1}$	3.5×10^{-1}	2.3×10^{-1}	$1.3 \times 10^{+1}$	3.1×10^{-1}	2.1×10^{-1}
$\Delta(\Phi_0)$	$2.0 \times 10^{+2}$	$3.6 \times 10^{+0}$	$1.7 \times 10^{+0}$	$2.0 \times 10^{+2}$	$3.8 \times 10^{+0}$	$1.7 \times 10^{+0}$	$2.1 \times 10^{+2}$	$3.8 \times 10^{+0}$	$1.6 \times 10^{+0}$
$\Delta(\alpha_0)$	1.8×10^{-1}	7.6×10^{-2}	6.5×10^{-2}	7.4×10^{-1}	7.2×10^{-2}	6.3×10^{-2}	$1.5 \times 10^{+0}$	7.8×10^{-2}	7.4×10^{-2}
$\Delta[\ln(\mu/D)]$	8.0×10^{-2}	7.8×10^{-2}	2.6×10^{-1}	7.1×10^{-2}	7.8×10^{-2}	2.6×10^{-1}	7.1×10^{-2}	7.7×10^{-2}	2.5×10^{-1}
$\Delta(t_0)\nu_0$	$3.1 \times 10^{+1}$	6.0×10^{-1}	2.9×10^{-1}	$3.2 \times 10^{+1}$	6.3×10^{-1}	2.9×10^{-1}	$3.2 \times 10^{+1}$	6.3×10^{-1}	2.8×10^{-1}

simplify the calculation further by ignoring the waveform modulation caused by LISA's motion (so they effectively pretend LISA is fixed at the center of our solar system), and by restricting attention to the waveform generated by just a single pair of LISA's arms. Thus, their waveforms are determined by only 5 parameters: an overall amplitude and phase, the two masses, and S/M^2. (Clearly, these simplifications were intended to make the Fisher matrix calculation essentially identical to the corresponding calculation for LIGO measurements of binary black hole coalescences.)

The fact that Ryan and Poisson effectively "toss out" most of the unknown parameters obviously tends to decrease the calculated error bars for the included parameters. On the other hand, their highly simplified waveforms obviously carry much less information than the true waveforms, which tend to have the opposite effect. *A priori*, it would seem difficult to guess whether the net effect of their approximations is to underestimate or overestimate $\Delta(\ln M)$, $\Delta(\ln \mu)$, and $\Delta(S/M^2)$. Therefore, unfortunately, their work does not seem to provide a useful check on ours. Nevertheless, Ryan's and Poisson's papers were an interesting first cut at the parameter estimation problem, and it seems interesting to compare our results to theirs.

For a $10 M_\odot$ CO and $10^6 M_\odot$ MBH, Ryan [2] obtains (at SNR=30): $\Delta(\ln M) = 1.8 \times 10^{-4}$, $\Delta(\ln \mu) = 1.9 \times 10^{-5}$, and $\Delta(S/M^2) = 4.9 \times 10^{-4}$. For the same masses and SNR, Poisson [22] states the results $\Delta(\ln M) = 6.7 \times 10^{-5}$, $\Delta(S/M^2) = 1.7 \times 10^{-3}$, and $\Delta(\ln \eta) = 1.8 \times 10^{-3}$, where $\eta \equiv \mu/M$. Since both Ryan and Poisson consider only the case $e_0 = 0$ and evaluate the Fisher matrix at the point $S/M^2 = 0$, their

results are most usefully compared to those in column 1 of our tables (i.e., $e_0 = 0.1$ and $S/M^2 = 0.1$). Our estimates of mass-determination accuracy are within roughly an order of magnitude of those quoted by Ryan and Poisson, and in fact lie between them. [Poisson does not quote a result for $\Delta(\ln \mu)$, but we can still compare our results directly to his by using

$$(\Gamma^{-1})^{\ln \eta, \ln \eta} = (\Gamma^{-1})^{\ln \mu, \ln \mu} + (\Gamma^{-1})^{\ln M, \ln M}$$
$$- 2(\Gamma^{-1})^{\ln \mu, \ln M}, \qquad (66)$$

which gives $\Delta \eta = 3.0 \times 10^{-4}$ for our case.] Our $\Delta(S/M^2)$ is ~ 10 times smaller than Ryan's and ~ 50 times smaller than Poisson's. We guess this is because in Ryan's and Poisson's waveforms the MBH spin affects only the orbital phase (whereas in the true waveforms the spin also controls the Lense-Thirring precession rate), leading them to overestimate the covariance of the spin with the two mass parameters, and hence to overestimate $\Delta(S/M^2)$.

D. Parameter extraction for a low-mass main-sequence star at Sgr A*

Finally, it is interesting to consider the parameter extraction accuracy for captures of LMMSs at the center of the Milky Way—the type of source whose anticipated SNR we discussed at the end of Sec. V. In Table IV we consider a few possible low-frequency orbits of a $0.06 M_\odot$ CO around the $2.6 \times 10^6 M_\odot$ MBH at the known distance and sky location of Sgr A*. We take D=7.9 kpc [44] and $\theta_S = 1.66749$; the value

for ϕ_S is picked arbitrarily, since the orbital location of the detector during the observation is unknown. The columns with eccentricity 0.43 and frequency 0.0035 mHz correspond to the orbit whose SNR output has been discussed above (in Fig. 16; also [41]), and assume the observation is made 10^6 years prior to plunge (just before tidal forces play an important role). In other columns we consider other possible values of the eccentricity, frequency, and MBH's spin. In calculating the Fisher matrix, we assumed a data integration time of 2 years.

Most of the values in the table result from inverting the full, 14D Fisher matrix. We find that the sky location of the source can be determined to within ~ 0.01 steradians. Unfortunately, the distance D to the source is entirely degenerate with the CO's mass, and the latter cannot be determined by itself from the GW signal. [This is as expected, since the accumulated effect of radiation reaction on the waveform phase, after observation time $T_{obs} \sim 1$ yr, is merely $\Delta \phi \sim \pi \dot{f} T_{obs}^2 \sim \pi f T_{obs}^2 / (10^6 \text{ yr}) \sim 10^{-2}$, for $f \sim 10^{-4}$ Hz.] Hence, the distance to the galactic center cannot be determined by the GW signal alone. However, in case where a detected GW signal appears to come from a capture at Sgr A* (as its sky position is consistent with the galactic center and its $\dot{f}$ is extremely small), one could use the value of D known from astronomical measurements, in order to determine the CO's mass μ. (Recent studies of stellar dynamics and RR Lyrae stars have specified D to within 4% [44]). The relative error in μ will then be approximately $\Delta[\ln(\mu/D)]$, or roughly 10%.

Once a source is confirmed to be at the galactic center, we may eliminate the sky location Ω_S (known exactly for Sgr A*) from the search, in order to improve the accuracy in determining the other parameters. We may also eliminate the CO's mass μ from the parameter list (while keeping μ/D)—again, because radiation reaction is negligible for this source.

To estimate the effect of this extra information on parameter extraction, we inverted the 11D minor of the Fisher matrix obtained by excluding the rows and columns associated with μ_S, ϕ_S, and $\ln \mu$. We found that this produces only a negligible improvement in measurement accuracy for the rest of the parameters, except for the MBH spin's direction; $\Delta \Omega_K$ decreases by a factor $\sim 1.5-3$. These improved values of $\Delta \Omega_K$ are given in the table as well, set off by parentheses.

The more interesting results of Table IV concern the intrinsic parameters of the galactic hole. We estimate that the mass of the central MBH (as well as the orbital eccentricity) could be determined to within relative error $\sim 4 \times 10^{-3}$ to 2×10^{-1}, i.e., comparable to or better than what is achieved today using astrometric methods. More impressive is the determination of the MBH's spin from the GW waveform to within ~ 0.005 (in units of M^2). It is hard for us to imagine an alternative method that would allow such an accurate measurement of the spin of the MBH at the Milky Way's center.

Finally, we point out that two approximations we have made—using PN equations of motion and a low-frequency approximation to LISA's response—should be really quite accurate for LMMS captures in our galaxy, since these inspirals are viewed at a very early stage (the orbits considered in Table IV have their pericenters at $\gtrsim 20M$), and most of the SNR comes from frequencies in the range 10^{-4}–10^{-3} Hz.

VII. CONCLUSIONS, CAVEATS, AND FUTURE WORK

Realistic capture orbits will be nonequatorial and somewhat eccentric, in general. We have made a first cut at answering some LISA data analysis questions, for such realistic cases.

The figures in Sec. V illustrate how the LISA SNR builds up over time for eccentric orbits (assuming there, for simplicity, that the MBH is nonspinning). These figures show that, for $\sim 10 M_\odot$ COs captured by $\sim 10^6 M_\odot$ MBHs, the last few years of inspiral can all contribute significantly to the SNR; for $\sim 1 M_\odot$ COs, the last few decades can be significant. Clearly, these long waveforms will increase the computational burden on matched-filtering detection schemes, and will exacerbate the self-confusion problem, since eccentric-orbit inspirals can deliver significant GW energy into the LISA band many years before they become individually detectable.

The tables in Sec. VI represent our attempt to estimate LISA's parameter estimation accuracy, for captures. For a typical source (a $10 M_\odot$ CO captured by a $10^6 M_\odot$ MBH at SNR of 30) we find that $\Delta(\ln M), \Delta(\ln \mu), \Delta(S/M^2)$, and Δe_0 will all be roughly $\sim 10^{-4}$, while $\Delta \Omega_S \sim 10^{-3}$ and $\Delta \Omega_K \sim 5 \times 10^{-2}$. Due to computational limitations, those results are based on measurements from only the final year prior to plunge. We naturally expect the measurement errors to decrease when one considers waveforms lasting the entire length of the LISA mission. In this sense, the numbers above represent rough upper limits to LISA's measurement accuracy. On the other hand, these estimates are based on a small sample of hand-picked points in parameter space. In the future we will improve these estimates by doing several-year integrations and a full Monte Carlo sampling of parameter space. Of course, our PN waveforms are probably not very accurate for COs very close to the plunge, but still the above estimates are the best ones available.

LISA has a reasonable chance of detecting LMMSs captured by the MBH at the center of our own galaxy. In this case, the sources will be detected $\sim 10^6$ yrs before the final plunge, when our PN waveforms and our low-frequency approximation to LISA's response function should both be more reliable. We find that, in a two-year integration, LISA could determine the magnitude and direction of our MBH's spin to within $\Delta(S/M^2) \sim 5 \times 10^{-3}$ and $\Delta \Omega_K \sim 10^{-2}$, and measure the mass of the infalling star to within $\sim 10\%$.

APPENDIX A: LENSE-THIRRING COMPONENT OF THE PERICENTER PRECESSION

At 1PN order, the piece of $\dot{\gamma} \equiv d\gamma/dt$ proportional to S is [30]

$$\dot{\gamma}|_{\propto S} = \frac{\hat{L}\cdot\hat{n}}{1-(\hat{L}\cdot\hat{n})^2}(\hat{L}\cdot\hat{n}\cos\lambda - \hat{S}\cdot\hat{n})\dot{\alpha} - 8\pi\nu(S/M^2)\cos\lambda(2\pi M\nu)(1-e^2)^{-3/2}, \quad (A1)$$

where $\dot{\alpha} \equiv d\alpha/dt$ is given in Eq. (31). [To derive this equation, use Eq. (4.4.45) of Brumberg [30], together with his Eqs. (4.4.41) and (4.4.33), and along with the definitions in Eqs. (1.1.6)–(1.10.10) therein.]

The expression (A1) is somewhat complicated (and worse, badly behaved as $\hat{L}$ approaches $\hat{n}$) due to the usual convention of defining γ as the angle from $\hat{x} \equiv [\hat{L}(\hat{L}\cdot\hat{n}) - \hat{n}]/(1-(\hat{L}\cdot\hat{n})^2)^{1/2}$ to pericenter. In the terminology of BCV [24], γ is neither wholly an intrinsic variable, nor an extrinsic one; it is of a mixed type. As explained in Sec. III, it is preferrable to introduce a pericenter angle that is defined purely intrinsically (i.e., without reference to the observer). Accordingly, we define $\tilde{\gamma}$ as the angle from $\hat{L}\times\hat{S}$ to the direction of pericenter. Then γ and $\tilde{\gamma}$ are related by

$$\gamma = \tilde{\gamma} + \beta, \quad (A2)$$

where β is given by Eq. (21). Not only is $\tilde{\gamma}$ wholly intrinsic, but we claim it also obeys a simpler (and better behaved) evolution equation, Eq. (29):

$$\dot{\tilde{\gamma}}|_{\propto S} = -12\pi\nu\cos\lambda(S/M^2)(2\pi M\nu)(1-e^2)^{-3/2}. \quad (A3)$$

The purpose of this Appendix is to prove this claim; i.e., we show that Brumberg's Eq. (A1) is indeed equivalent to our Eqs. (A3) and (A2).

Since it is obvious from the definitions that

$$\gamma_0 = \tilde{\gamma}_0 + \beta_0, \quad (A4)$$

what we need to prove is that

$$\dot{\beta} = \dot{\gamma} - \dot{\tilde{\gamma}}. \quad (A5)$$

From Eqs. (A1), (A3), and (31), and noting that $\dot{\gamma}$ and $\dot{\tilde{\gamma}}$ differ only in their piece $\propto S$, the RHS of Eq. (A5) becomes

$$\dot{\gamma} - \dot{\tilde{\gamma}} = \frac{\hat{L}\cdot\hat{n}}{1-(\hat{L}\cdot\hat{n})^2}(\hat{L}\cdot\hat{n}\cos\lambda - \hat{S}\cdot\hat{n})\dot{\alpha} + \cos\lambda\,\dot{\alpha}$$

$$= \frac{\cos\lambda - (\hat{L}\cdot\hat{n})(\hat{S}\cdot\hat{n})}{1-(\hat{L}\cdot\hat{n})^2}\dot{\alpha}. \quad (A6)$$

The left-hand side (LHS) of Eq. (A5) can be written as

$$\dot{\beta} = (\cos\beta)^{-1}d(\sin\beta)/dt, \quad (A7)$$

which, substituting for $\sin\beta$ and $\cos\beta$ from Eq. (21), yields

$$\dot{\beta} = \frac{[1-(\hat{L}\cdot\hat{n})^2]^{1/2}}{\hat{n}\cdot(\hat{S}\times\hat{L})}$$

$$\times \left\{ \frac{\cos\lambda(\hat{L}\cdot\hat{n})}{[1-(\hat{L}\cdot\hat{n})^2]^{1/2}} + \frac{(\cos\lambda\hat{L}\cdot\hat{n} - \hat{S}\cdot\hat{n})(\hat{L}\cdot\hat{n})(\hat{L}\cdot\hat{n})}{[1-(\hat{L}\cdot\hat{n})^2]^{3/2}} \right\}. \quad (A8)$$

Using now the evolution equation for $\hat{L}$, $\dot{\hat{L}} = \dot{\alpha}\hat{S}\times\hat{L}$, the last expression reduces to the RHS of Eq. (A6). This proves Eq. (A5), and hence Eq. (A3) is proved.

We note Eq. (A3) can also be seen as a special case of Eq. (A1), obtained by setting $\hat{n}$ equal to $\hat{S}$ in the latter. Finally, we also note that the term

$$\frac{\hat{L}\cdot\hat{n}}{1-(\hat{L}\cdot\hat{n})^2}(\hat{L}\cdot\hat{n}\cos\lambda - \hat{S}\cdot\hat{n})\dot{\alpha} \quad (A9)$$

in Eq. (A1) for $\dot{\gamma}$ is precisely the time derivative of what has been referred to in Ref. [23] (in the context of quasi-circular orbits) as the "Thomas precession phase." [The term (A9) is precisely the RHS of Eq. (28) in [23].] We see here that this "Thomas precession" term is really just the "$\hat{L}\times\hat{S}$ piece" of the pericenter precession [while the remainder of Eq. (A1) is the "$\hat{L}\cdot\hat{S}$ piece"].

APPENDIX B: RELATIVE MAGNITUDES OF PN CONTRIBUTIONS

Our goal here is to gauge the suitability of the PN formulas we use in evolving the CO's orbit within our model [Eqs. (27)–(30)]. The part of the inspiral relevant for detection by LISA takes place entirely within the highly relativistic region right next to the horizon, a regime where the validity of the PN expansion is normally to be suspected. Accordingly, we do not expect our PN expressions to show any convergence; we do wish to make sure, though, that truncating the PN expansion as in Eqs. (27)–(30) does not lead to a pathologi-
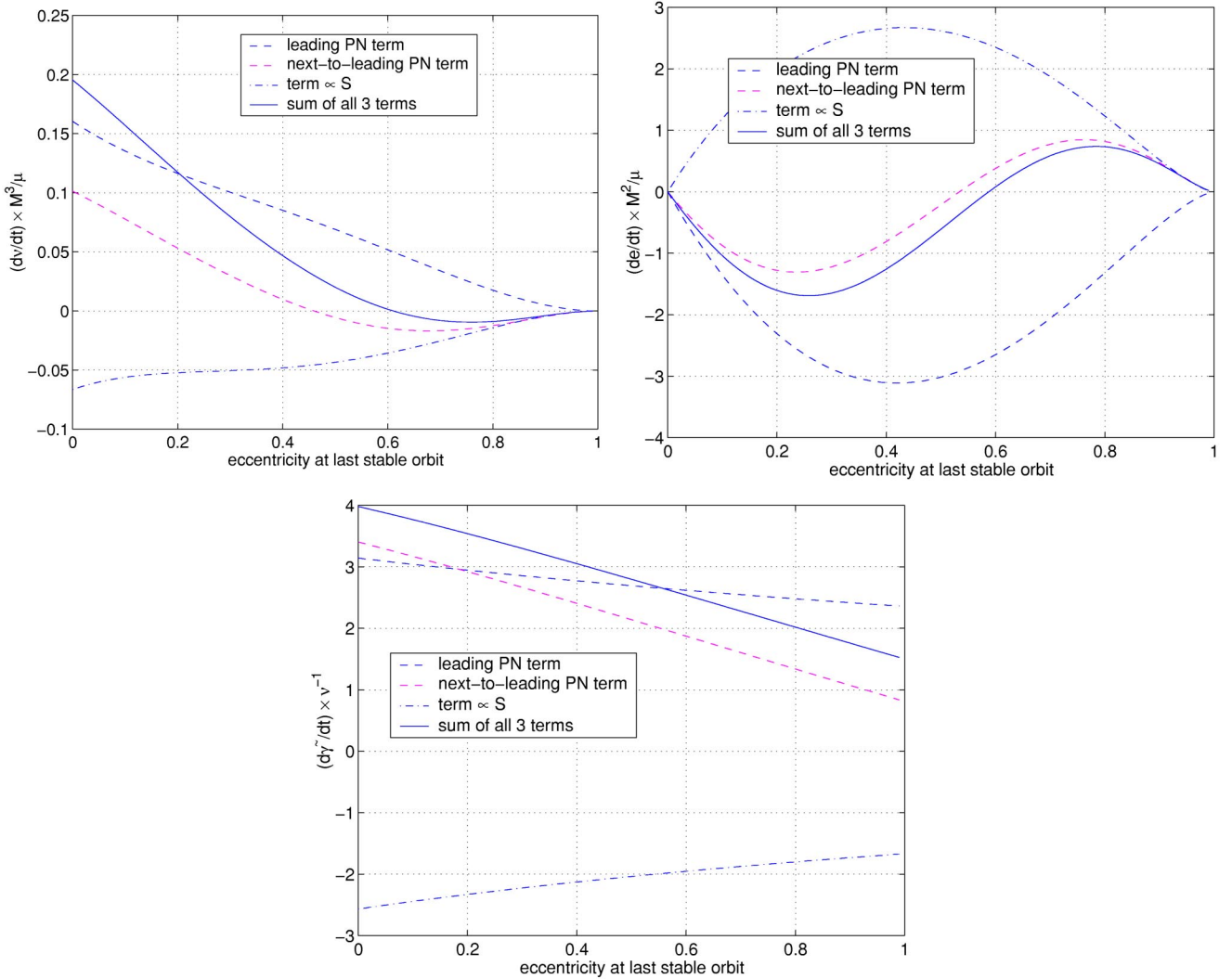
FIG. 17. Relative magnitudes of the various PN terms. The plots compare the contributions to $\dot\nu$ (upper left panel), $\dot e$ (upper right panel), and $\dot{\tilde\gamma}$ (bottom panel) from the various terms in the PN expressions (28)–(30), when the CO is at its last stable orbit. The various terms are of comparable magnitude, as expected in this "worse case." Note, though, that so long as $e_{\mathrm{LSO}} \lesssim 0.6$, the evolution of the orbital parameters at this order is free of potential pathologies [like "outspiral" ($\dot\nu < 0$), or a negative pericenter advance ($\dot{\tilde\gamma} < 0$)].

cal, unphysical evolution within the range of parameters relevant for our analysis.

In Fig. 17 we compare the magnitudes of the contributions from the various PN expansion terms to each of the time derivatives $\dot\nu$, $\dot e$, and $\dot{\tilde\gamma}$. We consider the "worse case," in which the CO has just reached the last stable orbit (LSO) and is about to plunge into the MBH. For simplicity, we take $(2\pi M\nu)_{\mathrm{LSO}} = [(1 - e^2)/(6 + 2e)]$, which is the value for a nonrotating MBH.

As expected, the various PN terms are of comparable magnitudes. Nevertheless, our evolution equations do not develop pathologies, so long as the LSO eccentricity is not too high. In particular, the orbital frequency increases monotonically (no "outspiral"!) and the eccentricity decreases monotonically (the orbit circularizes) throughout the entire evolution.

APPENDIX C: ESTIMATING THE EFFECT OF THE CO'S SPIN

In this appendix we refer to the spin of the MBH as $\vec S_1$, and denote by $\vec S_2$ the spin of the CO (in the rest of the paper the MBH's spin is denoted as simply $\vec S$). We present simple estimates of the effects of $\vec S_2$ on the orbital evolution, showing that, at any instant, these are smaller than the effects of $\vec S_1$ by an amount of order $(\mu/M)(\chi_2/\chi_1)$, where $\chi_1 \equiv |\vec S_1|/M^2$ and $\chi_2 \equiv |\vec S_2|/\mu^2$. This implies that over the course of the last ~ 1 yr of inspiral, the presence of the CO's spin modifies the accumulated orbital phase and precession angles by a few radians at most.

Clearly $\chi_1 < 1$. Theoretical upper limits on χ_2 are: $\chi_2 < 1$ when the CO is a BH; $\chi_2 \lesssim 2$ for a $1.4 M_\odot$ NS; and $\chi_2 \lesssim 5$ for a uniformly rotating, $0.5 M_\odot$ WD [45]. We do not

know the spin of any stellar-mass BH, but the NSs and WDs we find in nature are typically spinning at well below these maximum possible rates. Most known pulsars have $\chi_2 \sim 10^{-3} - 10^{-2}$ (recycled pulsars being the major exception), and it appears that WDs typically have $\chi_2 \sim 10^{-2}$ [46].

Our estimates here are based on low-order, post-Newtonian equations for circular-orbit binaries. Of course, the capture orbits of interest to us can be moderately eccentric in the LISA band, and they are sufficiently close to the MBH that higher-order post-Newtonian terms can be comparable in size to the lower-order terms that we do include. We expect that these higher-order PN terms, and modifications for $e \neq 0$, would modify our estimates on the effects of $\vec{S}_2$ by factors of order unity, but we anticipate that our PN estimates at least give the order of magnitude.

Two other recent works that consider the effect of the CO's spin on the capture waveform are by Hartl [47] and Burko [48].

1. Effect of $\vec{L} \cdot \vec{S}_2$ and $\vec{S}_1 \cdot \vec{S}_2$ terms on the waveform phase

For circular orbits, let $\omega \equiv 2\pi\nu + \dot{\gamma}$ be the angular frequency of the CO around the MBH. Defining Ψ to be the accumulated orbital phase from time t_i to t_f,

$$\Psi = \int_{t_i}^{t_f} \omega \, dt = \int_{\omega_i}^{\omega_f} \frac{\omega}{\dot{\omega}} \, d\omega, \quad (C1)$$

Kidder [49] finds that the change in the orbital phase Ψ due to nonzero $\vec{S}_2$ is

$$\Delta\Psi = \chi_2 \frac{125}{256} (\hat{L} \cdot \hat{S}_2) [(M\omega_i)^{-2/3} - (M\omega_f)^{-2/3}]$$
$$+ \chi_1 \chi_2 \left(\frac{1235}{1536} \hat{S}_1 \cdot \hat{S}_2 - \frac{3605}{1536} \hat{L} \cdot \hat{S}_1 \hat{L} \cdot \hat{S}_2 \right)$$
$$\times [(M\omega_i)^{-1/3} - (M\omega_f)^{-1/3}] + O(\mu/M). \quad (C2)$$

[Actually, Eq. (C2) refers to the case where the dot products $\hat{L} \cdot \hat{S}_2$, $\hat{L} \cdot \hat{S}_1$, and $\hat{S}_1 \cdot \hat{S}_2$ are constants (e.g., the case where these three angular momenta are all perfectly aligned or antialigned, so there is no Lense-Thirring precession). For the realistic case, where $\hat{L}$ and $\hat{S}_2$ undergo significant Lense-Thirring precession, these dot products would be replaced by appropriately weighted time averages.] For our case of inspiral orbits near plunge and $(t_f - t_i)$ of order a year, we have $[(M\omega_i)^{-1/3} - (M\omega_f)^{-1/3}] \sim 1 - 2$ and $[(M\omega_i)^{-2/3} - (M\omega_f)^{-2/3}] \sim 3 - 10$. Therefore, when χ_2 and χ_1 are of order one, $\Delta\Psi$ is at most a few radians, while Ψ itself is of order 10^6.

2. Effect of S_2 on pericenter precession, $d\gamma/dt$

The $\vec{S}_2$ contribution to $d\gamma/dt$ is given (to lowest nontrivial PN order) by Brumberg [30], in his Eqs. (4.4.41) and (4.4.45). We do not reproduce those equations here, but just note that the relevant terms are (for low eccentricity) of order $\chi_2(\mu/M)(M/r)^{3/2}\omega$ and $\chi_1\chi_2(\mu/M)(M/r)^2\omega$, respectively.

Therefore, the integrated effect of $\vec{S}_2$ on γ is $\Delta\gamma \sim \chi_2(\mu/M)N_{orb}$ radians, where N_{orb} is the number of orbits during the integration time. Hence, $\Delta\gamma$ is of order one radian for $\chi_2 \sim 1$ and typical values $\mu/M \sim 10^{-5}$ and $N_{orb} \sim 10^5$.

3. Effect of $\vec{S}_2$ on $\hat{S}_1$ and $\hat{L}$

We next estimate how $\vec{S}_2$ affects the Lense-Thirring precession. Our estimates are based on the following post-Newtonian precessional equations given by Apostolatos et al. [23], which were obtained by averaging the spin-orbit, spin-spin, and radiation reaction torques (all calculated to lowest nontrivial post-Newtonian order) over one complete orbit:

$$\dot{\vec{L}} = \frac{1}{r^3} \left[2\vec{S}_1 + \frac{3M}{2\mu}\vec{S}_2 \right] \times \vec{L}$$
$$- \frac{3}{2}\frac{1}{r^3} [(\vec{S}_2 \cdot \hat{L})\vec{S}_1 + (\vec{S}_1 \cdot \hat{L})\vec{S}_2] \times \hat{L} - \frac{32}{5}\frac{\mu^2}{r}\left(\frac{M}{r}\right)^{5/2} \hat{L},$$
$$(C3)$$

$$\dot{\vec{S}}_1 = \frac{2}{r^3}\vec{L} \times \vec{S}_1 + \frac{1}{r^3}\left[\frac{1}{2}\vec{S}_2 - \frac{3}{2}(\vec{S}_2 \cdot \hat{L})\hat{L} \right] \times \vec{S}_1, \quad (C4)$$

$$\dot{\vec{S}}_2 = \frac{3}{2r^3}\frac{M}{\mu}\vec{L} \times \vec{S}_2 + \frac{1}{r^3}\left[\frac{1}{2}\vec{S}_1 - \frac{3}{2}(\vec{S}_1 \cdot \hat{L})\hat{L} \right] \times \vec{S}_2. \quad (C5)$$

[Actually, Eqs. (C3)–(C5) are a simplified version of Eqs. (11a)–(11c) in Apostolatos et al., differing by fractional corrections of order μ/M.]

Two results that follow from Eqs. (C3)–(C5) are: (i) the two spin magnitudes, $|\vec{S}_1|$ and $|\vec{S}_2|$, are constants of the motion; and (ii) the total angular momentum, $\vec{J} = \vec{S}_1 + \vec{L} + \vec{S}_2$, is also constant, except for the orbital momentum that is radiated away:

$$\dot{\vec{J}} = -\frac{32}{5}\frac{\mu^2}{r}\left(\frac{M}{r}\right)^{5/2} \hat{L}. \quad (C6)$$

Therefore, $\Delta\vec{J}$—the total change in $\vec{J}$ over the observed inspiral—has magnitude of order $|\Delta\vec{L}| \sim (\mu M)$.

Combining this with the fact that the magnitudes of $\vec{S}_1$, $\vec{L}$, and $\vec{S}_2$ are roughly in the ratio

$$|\vec{S}_1| : |\vec{L}| : |\vec{S}_2| \sim \chi_1 : \mu/M : \chi_2(\mu/M)^2 \quad (C7)$$

(i.e., $|\vec{S}_1| \gg |\vec{L}| \gg |\vec{S}_2|$), one easily sees that the yearly change in the direction of $\vec{S}_1$ can be of order $\chi_1^{-1}(\mu/M)$ radians at most, no matter how $\hat{S}_2$ and $\hat{L}$ evolve. Thus our approximation of treating $\hat{S}_1$ as fixed, used throughout, remains valid when we include the effects of $\vec{S}_2$.

Finally, we consider the motion of $\hat{L}$. For $\vec{S}_2 = 0$, we have

seen that $\vec{L}$ simply precesses around $\vec{S}_1$ at rate $\dot{\alpha}$ given by Eq. (31). Because the terms in Eq. (C3) involving $\vec{S}_2$ are all smaller than the dominant $(2/r^3)\vec{S}_1 \times \vec{L}$ term by an amount of order $\chi_2(\mu/M)$ or $(\chi_2/\chi_1)(\mu/M)$, they represent a small perturbation on the simple precession picture, which can clearly be absorbed into a time-varying λ (the angle between $\hat{S}_1$ and $\hat{L}$) and a perturbed precession rate $\dot{\alpha}$. These extra terms in $\dot{L}$ are of order $\chi_2(\mu/M)(M/r)^{3/2}\omega$ and $\chi_1\chi_2(\mu/M)(M/r)^2\omega$, respectively—the same as for the $\vec{S}_2$ terms in $d\gamma/dt$—and so again integrate up to a yearly difference of order one radian at most.

4. Conclusion

If the CO's angular momentum is close to maximal (i.e., within a factor of a few), then the CO's spin is marginally relevant for the dynamics over time scales of the order of a year. However, if the CO is not rapidly rotating, or if one is just searching for short stretches (lasting ~ 2 weeks) of the waveforms in the data (e.g., as the first step of a hierarchical search), then the CO's spin can be safely neglected. (For such short stretches, in addition to the fact that the waveform phase errors from neglecting $\vec{S}_2$ are much less than one radian, it seems likely that these errors can be partially compensated for by errors in the other physical parameters.)

---

[1] K. Danzmann *et al.*, LISA- Laser Interferometer Space Antenna, Pre-Phase A Report, Max-Planck-Institut für Quantenoptic, Report MPQ 233, 1998.

[2] F.D. Ryan, Phys. Rev. D **56**, 1845 (1997).

[3] S. Sigurdsson and M.J. Rees, Mon. Not. R. Astron. Soc. **284**, 318 (1997); S. Sigurdsson, Class. Quantum Grav. **14**, 1425 (1997); M. Freitag, *ibid.* **18**, 4033 (2001).

[4] E. Poisson, gr-qc/0306052.

[5] http://www.tapir.caltech.edu/listwg1/

[6] P.C. Peters and J. Mathews, Phys. Rev. **131**, 435 (1963); P.C. Peters, Phys. Rev. **136**, B1224 (1964).

[7] C. Cutler, D. Kennefick, and E. Poisson, Phys. Rev. D **50**, 3816 (1994).

[8] K. Glampedakis and D. Kennefick, Phys. Rev. D **66**, 044002 (2002).

[9] S.A. Hughes, Phys. Rev. D **61**, 084004 (2000).

[10] C. Cutler, Phys. Rev. D **57**, 7089 (1998).

[11] N.J. Cornish and L.J. Rubbo, Phys. Rev. D **67**, 022001 (2003); **67**, 029905(E) (2003).

[12] D. Richstone *et al.*, Nature (London) **395**, A14 (1998).

[13] J. Kormendy and K. Gebhardt, in *Proceedings of 20th Texas Symposium on Relativistic Astrophysics*, edited by H. Martel and J. C. Wheeler (AIP, New York, 2002), astro-ph/0105230.

[14] D. Hils and P.L. Bender, Astrophys. J. Lett. **445**, L7 (1995).

[15] E. S. Phinney (unpublished).

[16] L.S. Finn and K.S. Thorne, Phys. Rev. D **62**, 124021 (2000).

[17] K. Glampedakis, S.A. Hughes, and D. Kennefick, Phys. Rev. D **66**, 064005 (2002).

[18] M. Freitag, Astrophys. J. Lett. **583**, L21 (2003).

[19] Members of WG1 communicate through regular telecons. Progress reports are posted on the WG1 website, Ref. [5].

[20] M. Peterseim, O. Jennrich, and K. Danzmann, Class. Quantum Grav. **13**, 279 (1996).

[21] A. Vecchio, astro-ph/0304051.

[22] E. Poisson, Phys. Rev. D **54**, 5939 (1996).

[23] T. Apostolatos, C. Cutler, G.J. Sussman, and K.S. Thorne, Phys. Rev. D **49**, 6274 (1994).

[24] A. Buonanno, Y. Chen, and M. Vallisneri, Phys. Rev. D **67**, 024016 (2003).

[25] C. W. Misner, K. S. Thorne, and J. A. Wheeler, *Gravitation* (Freeman, San Francisco, 1973), Chap. 33.

[26] M. Tinto, F.B. Estabrook, and J.W. Armstrong, Phys. Rev. D **65**, 082003 (2002).

[27] K.S. Thorne, in *300 Years of Gravitation*, edited by S.W. Hawking and W. Israel (Cambridge University Press, Cambridge, England, 1987), pp. 330–458.

[28] D.M. Marković, Phys. Rev. D **48**, 4738 (1993).

[29] W. Junker and G. Schäfer, Mon. Not. R. Astron. Soc. **254**, 146 (1992).

[30] V. A. Brumberg, *Essential Relativistic Celestial Mechanics* (IOP, Bristol, 1991).

[31] F.D. Ryan, Phys. Rev. D **53**, 3064 (1996).

[32] B.M. Barker and R.F. O'Connell, Phys. Rev. D **12**, 329 (1975).

[33] L. Blanchet, G. Faye, B.R. Iyer, and B. Joguet, Phys. Rev. D **65**, 061501(R) (2002).

[34] C. Cutler and E.E. Flanagan, Phys. Rev. D **49**, 2658 (1994).

[35] S.A. Hughes, Mon. Not. R. Astron. Soc. **331**, 805 (2002).

[36] B. Abbott *et al.* (unpublished).

[37] A.J. Farmer and E.S. Phinney, Mon. Not. R. Astron. Soc. **346**, 1197 (2003).

[38] G. Nelemans, L.R. Yungelson, and S.F. Portegies Zwart, Astron. Astrophys. **375**, 890 (2001).

[39] R.F. Webbink and Z. Han, in *Proceedings 2nd International LISA Symposium*, edited by W. Folkner (AIP, New York, 1998), astro-ph/0105230.

[40] N.J. Cornish, gr-qc/0304020.

[41] M. Freitag, in the proceedings of ''The Astrophysics of Gravitational Wave Sources,'' a workshop held at the University of Maryland, 2003, astro-ph/0306064.

[42] W. H. Press, S. A. Teukolsky, W. T. Vetterling, and B. P. Flannery, *Numerical Recipes* (Cambridge University Press, Cambridge, England, 1992).

[43] C. Cutler and A. Vecchio, in *Proceedings 2nd International LISA Symposium*, edited by W. Folkner (Ref. [39]).

[44] D.H. McNamara, J.B. Madsen, J. Barnes, and F.B. Ericksen, Publ. Astron. Soc. Pac. **112**, 202 (2000).

[45] S. L. Shapiro and S. A. Teukolsky, *Black Holes, White Dwarfs, and Neutron Stars* (Wiley-Interscience, New York, 1983).

[46] S.D. Kawaler, astro-ph/0301539.

[47] M.D. Hartl, Phys. Rev. D **67**, 104023 (2003).

[48] L. Burko, Phys. Rev. D **69**, 044011 (2004).

[49] L.E. Kidder, Phys. Rev. D **52**, 821 (1995).